PNAS
www.pnas.org

Supplementary Information for

Strong evidence for a weakly oxygenated ocean–atmosphere system during the Proterozoic

Changle Wang, Maxwell A. Lechte, Christopher T. Reinhard, Dan Asael, Devon B. Cole, Galen P. Halverson, Susannah M. Porter, Nir Galili, Itay Halevy, Robert H. Rainbird, Timothy W. Lyons, Noah J. Planavsky

Corresponding authors: Changle Wang, Maxwell A. Lechte
Email: wangcl@mail.iggcas.ac.cn; maxwell.lechte@mail.mcgill.ca

This PDF file includes:

Other supplementary materials for this manuscript include the following:

Supplementary Materials and Methods

Materials. Proterozoic ironstone samples were collected from surface outcrop and/or drill holes in seven localities: Northern Territory (Australia; Sherwin Formation); North China (China; Chuanlinggou Formation); Wisconsin (USA; Freedom Formation); Grand Canyon, Arizona (USA; Galeros Formation); Amundsen Basin, Northwest Territories (Canada; Nelson Head Formation); Wernecke Mountains, Yukon (Canada; McClure Formation), and Great Slave Lake, Northwest Territories (Canada; Gibralter Formation). We also collected samples of several Phanerozoic ironstones and Holocene iron-rich sediments from surface outcrop to compare to their Proterozoic counterparts, given that Phanerozoic ironstones have been extensively studied (*1*-*3*). Additional ironstone and iron-rich samples (such as the Clinton Group and Villers Formation ironstones and bog ore) were provided by the University of Cincinnati Museum and the Yale Peabody Museum collections. Information on each sample is available in the museum database using the provided repository numbers. All samples used in this study will be archived in the Yale Peabody Museum upon publication of this work. We provide information about the geological setting, petrography, and sedimentology of these Proterozoic and Phanerozoic ironstones below.

Petrographic analysis. Ironstone samples were prepared as polished thick (~100 μm) thin sections for petrographic analysis. These samples were analyzed by reflected light microscopy and Raman spectroscopy at the Department of Earth and Planetary Sciences (McGill University). Following Raman analysis, samples were carbon coated and studied using scanning electron microscopy (SEM) carried out on a JEOL 8900 electron microprobe at the Department of Earth and Planetary Sciences.

Bulk rock geochemical analyses. Samples were cut with a diamond edge rock saw to remove weathered surfaces, and subsequently crushed in an agate mill to a fine powder. Approximately 50 mg of sample powder was dissolved in Teflon beakers using concentrated HF and HNO_3 for 24 hours, dried down, and subsequently dissolved again using Aqua Regia at a ratio of 1 part HNO_3 to 3 parts HCl for 48 hours. If undigested sample powder remained after this step, samples were centrifuged to remove insoluble residue and the supernatant was carefully transferred into Teflon beakers and dried. Final residues were dissolved in 5 ml 6 N HCl for stock solutions for geochemical analyses. A small aliquot (~10 μl) out of 5 ml 6 N HCl was then dried down and brought up to 4 ml with 5% HNO_3 containing 1 ppb Indium. The resulting solutions were analyzed in the Department of Geology and Geophysics at Yale University by inductively coupled plasma mass spectrometry (ICP-MS; ThermoFisher Scientific Element XR) to determine selected major and trace elements using a standard sample introduction system. Measurement precision was generally better than 5% for major and trace elements and USGS geostandards BHVO-2 and NOD-A-1 processed along with samples during each run are within 10% of reported values. In order to determine the pyrite content of siliciclastic rocks, sulfide was liberated during chromium reduction via the method outlined in Canfield et al. (*4*), and the mass was measured gravimetrically (assuming FeS_2 stoichiometry) after trapping as Ag_2S.

Iron isotope analyses. Sample solutions prepared for bulk rock geochemical analyses were selected for iron isotope analyses and purified using ion-exchange chromatography with AG-MP-1M resin (100-200 mesh) (methods modified from ref. (*5*)). The resin was preconditioned in HCl medium by running H_2O, 0.24 N HCl, 0.5 N HNO_3, and 7 N HCl. The sample solution containing 8 μg Fe was dried down and finally dissolved with 1 ml 7 N HCl + 0.001% H_2O_2. After it was loaded on the column, matrix elements were eluted with 7 N HCl, whereas Fe(III) was strongly adsorbed on the resin and was quantitatively retained. Iron was subsequently eluted in 2 N HCl and 0.5 N HNO_3, with a procedural yield of >97%. Iron isotopes were measured using a Thermo Neptune Plus MC-ICP-MS at the Yale Metal Geochemistry Center. Iron isotope results were bracketed by, and reported relative to, the IRMM-14 standard in standard delta notation in per mil (‰) as:

$$\delta^{56}Fe = [(^{56}Fe/^{54}Fe)_{sample}/(^{56}Fe/^{54}Fe)_{standard} - 1] \times 1000 \quad \text{(S1)}$$

The total procedural Fe blank was less than 40 ng, which is negligible compared to the amount of Fe in the samples. Analytical accuracy and precision of the measured $\delta^{56}Fe$ values were assessed by repeated processing and analysis of USGS reference material BHVO-2 and NOD-A-1 as unknowns with samples. Average sample 2σ was 0.022‰. Measured $\delta^{56}Fe$ values were 0.11 ± 0.14‰ (n = 40) for BHVO-2 and -

0.30 ± 0.15‰ (n = 40) for NOD-A-1, which are within error of the published values for these two standards (*6, 7*). In addition to the standards, three unknown samples were processed in duplicate and all yielded 2σ values <0.03‰.

Isotopic and kinetic model of iron oxidation. In order to estimate the extent of Fe(II) oxidation based on an observed δ^{56}Fe value, we start with a conventional Rayleigh distillation model:

$$\delta^{56}_{react} = 1000 \cdot \left\{ \left[\left(1 + \frac{\delta^{56}_{in}}{1000} \right) \cdot f_{reac}^{\alpha - 1} \right] - 1 \right\} \quad \text{(S2)}$$

$$\delta^{56}_{inst} = \delta^{56}_{react} + (\alpha - 1) \cdot 1000 \quad \text{(S3)}$$

$$\delta^{56}_{total} = 1000 \cdot \left[\left(1 + \frac{\delta^{56}_{in}}{1000} \right) \cdot \left(\frac{1 - f_{reac}^{\alpha}}{1 - f_{reac}} \right) - 1 \right] \quad \text{(S4)}$$

Here, δ^{56}_{in}, δ^{56}_{react}, δ^{56}_{inst}, and δ^{56}_{total} refer to the δ^{56}Fe composition of the input, the reactant pool, the instantaneous product of Fe(II) oxidation, and the total (cumulative) product of Fe(II) oxidation, respectively. f_{reac} refers to the fraction of Fe(II) that has been oxidized and α refers to the combined fractionation factor for Fe(II) oxidation and precipitation of Fe oxides. We utilize data from bulk rock samples from ironstones interpreted to be deposited due to water column Fe(II) oxidation; therefore, if an observed isotope value is ^{56}Fe-enriched relative to the range of likely input values ($-0.5 < \delta^{56}_{in} < +0.3$ ‰), we use the Rayleigh model for a cumulative product. However, some ironstones feature negative δ^{56}Fe values, requiring separation of distinct iron pools during fractionation. As such, if an observed isotope value is ^{56}Fe-depleted relative to this range of input values, we use the Rayleigh model for an instantaneous product. If an observed isotope value falls within the range of possible input values, it is taken as indistinguishable from quantitative Fe(II) oxidation. We assume three different values for the fractionation factor (α = 1.001, 1.002, and 1.003).

Our model then compares the estimates of fractional Fe(II) oxidation based on the observed isotope data to those derived from a kinetic model of Fe(II) oxidation (*8*):

$$\frac{d[\mathrm{Fe}^{2+}]}{dt} = k_{ox}[\mathrm{Fe}^{2+}][\mathrm{O}_2][\mathrm{OH}^-]^2 \quad \text{(S5)}$$

In this model, Fe^{2+} represents dissolved ferrous iron, O_2 is dissolved oxygen, OH^- is the hydroxide ion abundance, and square brackets denote concentration. The term k_{ox} is an overall rate constant for the Fe(II) oxidation process, which is scaled to temperature (T) and ionic strength (I) according to:

$$\log k = \log\left(21.56 - \frac{1545}{T} \right) - 3.29 I^{0.5} + 1.52 I \quad \text{(S6)}$$

Equation S5 above can be solved to yield the fraction of dissolved Fe^{2+} remaining over time according to:

$$\frac{[\mathrm{Fe}^{2+}]_t}{[\mathrm{Fe}^{2+}]_0} = \exp[-\lambda t] \quad \text{(S7)}$$

where:

$$\lambda = k_{ox}[\mathrm{O}_2][\mathrm{OH}^-] \quad \text{(S8)}$$

According to Equations S5–8, we can estimate the relative fraction of Fe^{2+} consumed by oxidation over time given an assumed temperature (T), ionic strength (I), dissolved oxygen concentration ($[O_2]$), and seawater pH (e.g., $[OH^-]$). Then, given a timescale available for oxidation (t), we can estimate a discrete fractional Fe(II) oxidation, e.g.:

$$f_{ox} = 1 - \frac{[\mathrm{Fe}^{2+}]_t}{[\mathrm{Fe}^{2+}]_0} \quad \text{(S9)}$$

To estimate the timescale available for Fe(II) oxidation, we use estimates of residence time in the mixed layer from high-resolution general circulation model experiments (*9*). Specifically, we fit lognormal distributions for the mixed layer residence times of all grid cells for two assumed mixed layers depths (50 m and 90 m; Fig. S1). We run our oxidation model stochastically, sampling from random (uniform)

distributions for T (15–35 ºC), pH (6.8–8.8), and lognormal distributions for oxidation timescale (see Fig. S1). Dissolved O_2 concentrations are calculated at gas-exchange equilibrium based on an assumed atmospheric pO_2, with solubility corrections for temperature and salinity (*10*). We run the model 10^5 times at each assumed atmospheric pO_2 value, generating the statistical distributions shown in Figure 3.

Importantly, even with entirely different modelling approaches, our ironstone Fe isotope data point to the same conclusion: low O_2 concentrations in shallow seawater. Czaja et al. (*11*) presented a one-dimensional dispersion–reaction model for Fe(II) oxidation and associated Fe isotope fractionation, which can be used to convert $\delta^{56}Fe$ values to estimates for contemporaneous seawater O_2 concentrations. This model has been subsequently developed and widely applied to other deposits by later authors (*12-17*). If we input our ironstone data into this modelling framework, the positive $\delta^{56}Fe$ values of the ironstone record require very low (nanomolar) O_2 concentrations in the photic zone, which is much lower than maximum constraints on O_2 provided by our model (Fig. 4). The estimates the dispersion–reaction model are much lower than the constraints of our model because we allow for longer residence times in the surface ocean and we allow for slower Fe(II) oxidation rates at a given O_2 level (given the potential of a low marine pH). In any case, regardless of the model specifics, both models give the same answer: that the O_2 levels of the atmosphere–ocean system were extremely low.

Flux calculations for air–sea gas exchange and Fe(II) upwelling. In order to test the hypothesis that mid-Proterozoic surface waters would have remained close to equilibrium with the overlying atmosphere during ironstone deposition, we compare the flux of O_2 supplied by air–sea gas exchange to estimates for the flux of Fe(II) that could have been supplied by upwelling of ferruginous seawater. With greater upwelling rates, nutrient flux increases, which results in a concomitant increase in local O_2 production and can lead to O_2 supersaturation in surface waters in modern upwelling coastal margins (*18*). In order to provide a conservative estimate for the Fe(II) concentrations and upwelling rates required to quantitatively oxidize the surface water O_2 supplied by air–sea gas exchange, we perform our calculations assuming that local O_2 production was negligible.

Air–sea gas-exchange rates are commonly calculated using a two-layer (film) model whereby the gas and liquid bodies are assumed to be well mixed, and the steady-state flux of O_2 through the interface (e.g., the ocean surface) is proportional to the concentration gradient via a gas transfer velocity (*19, 20*). The net flux of O_2 (F_{O2} in mmol m^{-2} day^{-1}) across the air–sea interface can therefore be related to pO_2 via:

$$F_{O2} = k_{O2} \cdot \left(H_{O2} \cdot pO_2 - \left[O_2 \right] \right) \quad \text{(S10)}$$

where k_{O2} is the gas transfer velocity (in cm h^{-1}), $[O_2]$ represents surface seawater O_2 concentrations and H_{O2} is the Henry's law solubility constant (in mol m^{-3} atm^{-1}), defined by the ratio of the equilibrium concentration of O_2 in seawater and atmospheric pO_2.

Therefore, the movement of O_2 across the interface is limited by k_{O2}, which is related to a number of environmental factors including concentration gradients, wind speed, turbulence, and bubbles (*21*). However, most of the boundary layer processes that govern air–sea gas transfer, such as turbulence and shear, are strongly influenced by wind speed (*22*). We calculate k_{O2} following the method of Wanninkhof (*23*), whereby k_{O2} is a function of the mean squared wind speed (determined at 10 m altitude; U in m s^{-1}), and the square root of the dimensionless Schmidt number (Sc), which describes the relationship between the kinematic viscosity of water and the molecular diffusion coefficient of gases (*23*). We employ a value of 7.3 m s^{-1} for U as determined from a Rayleigh distribution based upon the Cross Calibrated Multi-Platform (CCMP; 1990–2009) wind product (*24*). However, wind products from different calculations show significant variability (*25*), which will affect the calculated gas transfer velocity. In order to reduce uncertainties and biases in the global wind speed assumption, a coefficient is introduced to the gas transfer velocity calculation (*26*). The optimal coefficient of gas transfer, obtained from an inverse modelling approach using the CCMP winds and a general circulation model (*23, 26*), is 0.251 (cm h^{-1}) (m s^{-1})$^{-2}$. Accordingly, the transfer velocity of O_2 across the ocean surface can be calculated according to:

$$k_{O2} = 0.251 \cdot U^2 \cdot (Sc/660)^{(-0.5)} \quad \text{(S11)}$$

This propagated uncertainty of this k_{O2} calculation is estimated to be 20 % (*23*), and this calculation—and the dependence of gas exchange on wind speed—is supported by empirical measurements from several ocean gas-exchange studies (*27*). The relationship described in Equation S11 is considered to apply to

instantaneous (short-term) winds, which may underestimate the gas-transfer velocity of long-term averaged winds; according to Wanninkhof (*23*), a correction can be applied by multiplying by a factor of 1.26.

The flux of O_2 from the atmosphere to the ocean can be calculated by using only the downward (i.e., positive) term from Equation S10. The values of H_{O_2} and Sc depend upon temperature and salinity—here we calculate H_{O_2} (according to Ref. *10*) and Sc (*28*) for seawater (35 ‰ salinity) at 15–35 ºC. Using these parameters, and converting the units to mmol m^{-2} day^{-1}, we present the results for the calculated downward flux of O_2 at a range of values for T and atmospheric pO_2 in Fig. S2.

Following the approach of Coale et al. (*29*), the vertical flux of Fe(II) (F_{Fe} in mmol m^{-2} day^{-1}) that could have been delivered to the mid-Proterozoic surface ocean can be described as:

$$F_{Fe} = w_u \cdot \left[Fe^{2+}\right] + K_z \cdot \frac{d\left[Fe^{2+}\right]}{dz} \quad \text{(S12)}$$

where w_u is the mean vertical velocity of upwelling seawater (m day^{-1}), $[Fe^{2+}]$ is the dissolved Fe(II) concentration of deep waters (μM), and K_z is the vertical diffusivity coefficient (m^2 day^{-1}). Because the vertical flux due to diffusion is small compared to that supplied by upwelling (*30*), and requires several other assumptions about the mid-Proterozoic water column, we can simplify the comparison to the downward flux of O_2 by considering only the upwelling flux of Fe(II) in terms of two variables: w_u and $[Fe^{2+}]$.

In the modern oceans, the regions of greatest upwelling are around the equator and in western coastal regions of continents (i.e., the eastern zones of oceans) in the tropics (*31*). Upwelling rates are difficult to measure due to the low velocities involved, and rely upon tracer observations (e.g., *32, 33*). Estimates for globally averaged w_u are approximately 0.01 m day^{-1} (*32*), and w_u is typically estimated to be 0.1–1.0 m day^{-1} in upwelling zones (*34-37*). Maximum w_u values during periods of enhanced upwelling have been suggested to exceed 2.5 m day^{-1} (*38-40*), although these estimates are typically associated with large uncertainties (particularly for coastal environments; *39*). Estimates based on tracer studies are typically presented over seasonal timescales, whereas average upwelling rates on longer (annual) timescales are likely more relevant given that our data from whole-rock geochemical analyses of sedimentary rocks represents a time-integrated record. Using an ocean dynamics model, Froyland et al. (*41*) estimate average w_u values for modern equatorial regions and coastal upwelling zones (on 48 week timescales) of approximately 0.1–0.2 m day^{-1}. For other models of biogeochemical cycling in modern coastal upwelling zones, Ianson and Allen (*42*) used 0.785 m day^{-1} as a reasonable value for w_u, whereas Canfield (*43*) used a range of 0.06–1.7 m day^{-1} with w_u values between 0.24–0.72 m day^{-1} considered most likely. For comparison to deep time work, Piper and Link (*44*) present a model for a model for seawater circulation in a Permian basin and estimate that upwelling rates were ~0.23 m day^{-1} (based upon phosphorite accumulation rates), a value comparable w_u values obtained for modern analogs (*45*). Trabucho Alexandre et al. (*46*) used a global coupled climate model to estimate similar upwelling rates of ~0.25 m day^{-1} during Cretaceous oceanic anoxic events, with maximum upwelling up to 1.3 m day^{-1} along the equatorial divergence zone. For our whole-rock geochemical data from ironstones, we suggest that w_u values of ~0.2–0.3 m day^{-1} are a reasonable estimate for the average (time-integrated) upwelling rates of mid-Proterozoic upwelling zones, with a likely upper bound of ~0.8 m day^{-1} for periods of enhanced upwelling.

The upper limit on deep marine $[Fe^{2+}]$ levels of the mid-Proterozoic is not well constrained. The lack of massive banded iron formations in the mid-Proterozoic stratigraphic record has led previous researchers to infer that marine $[Fe^{2+}]$ levels were much lower than in earlier periods (*47, 48*). Thermodynamic modelling has been used to suggest that $[Fe^{2+}] > 50$ μM is required for the formation of banded iron formations, and that this value therefore represents a maximum constraint on seawater $[Fe^{2+}]$ in the mid-Proterozoic (*49*). Given evidence for the persistence of widespread ferruginous conditions during the mid-Proterozoic (*50*), there is extensive debate regarding the buffering of $[Fe^{2+}]$ in ferruginous deep waters by authigenic ferrous precipitates such as siderite (*47, 51*), vivianite (*52*), greenalite (*53, 54*), and green rust (*55, 56*). If seawater was in equilibrium with siderite then deep marine $[Fe^{2+}]$ was likely <200 μM (*52*), however, siderite precipitation from seawater may require high levels of supersaturation and could have been kinetically inhibited in Precambrian oceans (*57*). Evidence from experimental and modern analog studies shows that Fe(II)–Fe(III) hydroxy salts (green rust) could have readily formed in Proterozoic ferruginous oceans and may have exerted a control on deep marine $[Fe^{2+}]$ (*55, 56*). Modelling results indicate that if siderite precipitation does not require supersaturation, deep marine $[Fe^{2+}]$ levels are modulated at ~1–10 μM due to deep marine siderite precipitation and the formation of green rust and/or Fe(III) oxyhydroxides in surface waters (*55*). If seawater $[Fe^{2+}]$ was instead limited by greenalite solubility

then concentrations may have been much higher (*57*), with the maximum [Fe^{2+}] determined by greenalite solubility ranging from ~1600 μM at pH 7.2 down to ~200 μM at pH 7.7 and ~20 μM at pH 8 (*54*). The precipitation of Fe phosphates such as vivianite have also been proposed to have exerted an important influence on marine chemistry, and geochemical modelling suggests vivianite reaches saturation close to ~220 μM [Fe^{2+}] at pH 7.75 (*52*). However, the various constraints on [Fe^{2+}] based upon Fe mineral solubility depend heavily on pH, and previous estimates for Precambrian span a wide range (*58*). Accordingly, we consider a wide range of seawater [Fe^{2+}] in our upwelling flux calculation (Fig. S2).

The oxidation of seawater Fe(II) can take place via abiotic reaction with O_2 (and secondary reactive oxygen species) under oxygenated conditions, which can be expressed via the stoichiometric equation:

$$4Fe^{2+} + O_2 + 10H_2O \rightarrow 4Fe(OH)_3 + 8H^+ \quad \text{(S13)}$$

Iron oxidation can also take place via direct biological pathways such as the reaction with O_2 under microaerobic conditions mediated by chemoautotrophs (*59*):

$$12Fe^{2+} + O_2 + 2CO_2 + 32H_2O \rightarrow 2[CH_2O] + 12Fe(OH)_3 + 24H^+ \quad \text{(S14)}$$

where [CH_2O] represents biomass. Iron oxidation can also take place in the absence of O_2, such as via anoxygenic photosynthesis (*60*).

If we assume that atmospheric O_2 can oxidize upwelling seawater Fe(II) at a molar ratio of 1:4 (*8, 61*), then the upwelling Fe(II) flux needs to be more than four times greater than the downward flux of O_2 from the atmosphere in order to exhaust surface water O_2 sourced from the atmosphere (ignoring any O_2 from local production). As shown in Figure S2, even with high w_u values (0.8 m day^{-1}) and [Fe^{2+}] values (25–250 μM) considered, the downward flux of O_2 from the atmosphere cannot be exhausted by upwelling Fe(II) unless pO_2 is also low (requiring less than approximately 3 % PAL). At pO_2 = 1% PAL (and T = 25ºC), the downward flux of O_2 from the atmosphere is approximately 14 mmol m^{-2} day^{-1}, requiring a Fe flux exceeding 56 mmol m^{-2} day^{-1}. For deep marine [Fe^{2+}] < 70 μM, the Fe(II) flux is insufficient even during enhanced upwelling (w_u < 0.8 m day^{-1}; Fig. 2). At w_u values of 0.25 m day^{-1}—comparable to long-term averaged values calculated for modern (*41*) and ancient (*44, 46*) upwelling zones—deep marine [Fe^{2+}] would need to be extremely high (in excess of 224 μM; Fig. 2). Therefore, at pO_2 = 1% PAL, the upwelling Fe(II) flux is only comparable to that of the atmospheric flux of O_2 at very high values for w_u and [Fe^{2+}] (Fig. S2). Therefore, the ironstone Fe isotopic evidence for low seawater [O_2] is most easily explained by low atmospheric pO_2 (i.e., pO_2 ≤ 1 % PAL), rather than the depletion of surface water O_2 due to upwelling marine Fe(II).

Statistical analyses of iron isotope data. A range of statistical analyses was employed to test the hypothesis that there was a statistically significant change in ironstone Fe isotope composition in the late Proterozoic, following the approach of Sperling et al. (*62*). The ironstone Fe isotope data were classified into three time bins: ca. 1880–900 Ma (i.e., all Proterozoic ironstone data except the Galeros Formation; n = 195), ca. 470–0 Ma (i.e., all Phanerozoic ironstones and ferruginous sediments; n = 52), and the ca. 750 Ma Galeros Formation ironstone (n = 14). Anderson-Darling tests indicate that the Proterozoic and Phanerozoic ironstone data have strongly skewed distributions, necessitating non-parametric statistical analyses. Analysis of variance (one-way ANOVA and Kruskal-Wallis) methods were used to query whether the generated ironstone data from the three time bins had a common mean. Pairwise multiple comparisons (Tukey's honest significant difference and Wilcoxon tests) were then used to identify which bins were statistically significant. The results of these analyses (Dataset S4) show that filtered Proterozoic ironstone data is significantly different from the Galeros Formation and Phanerozoic ironstone data. The distributions of the Galeros Formation ironstone and Phanerozoic ironstone Fe isotope data are not significantly different. We suggest that these results indicate a shift from partial to quantitative Fe(II) oxidation in shallow seawater between 900–750 Ma.

Supplementary Information Text

Geological setting.

The ca. 1880 Ma Gibralter Formation, Kahochella Group (Canada)

The Orosirian Kahochella Group is located in the Slave craton and belongs to the Great Slave Supergroup, which is more than 12-km thick and consists of weakly metamorphosed sedimentary and volcanic rocks. This supergroup represents the depositional history of the Great Slave basin at 2100-1800 Ma, and is subdivided into five units (from lowermost to uppermost: the Union Island; Sosan; Kahochella; Pethei; and Christie Bay groups; *63*). The granular ironstone occurs in the Gibralter Formation, the lowermost unit of the Kahochella Group, and has undergone lower greenschist facies metamorphism.

The Gibralter Formation is dominated by red shale, with minor interbeds of calcareous shale and red siltstone, interpreted to have been deposited in a nearshore marine setting (*63*). The ironstone horizons form 30 cm thick interbeds and lenses of iron oolite between cross-bedded sandstones and are associated with shallow marine shales (Fig. S3), along with andesitic, pyroclastic volcanic rocks that host Cu-sulphide mineralization (*64*). The horizons feature iron ooids of variable size (typically ranging from <100 μm to 2 mm in diameter; Fig. S5a) composed of fine, concentric hematite laminae (locally weathered to goethite). The iron ooids are hosted by coarse, angular quartz sand with a fine-grained hematitic matrix. In places, iron ooids are broken intraclasts; some fragments form the cores of larger, composite ooids or pisoids, indicating significant mechanical reworking prior to deposition. These oolitic horizons are associated with red shales, and the observation of cross-bedded, granular hematite as well as intraformational conglomerates and stromatolites, indicates deposition in a shallow marine environment (*63*).

The granules within the Gibralter Formation are composed dominantly of chert and densely compacted nanoscopic grains of red or grey hematite (*65*). Such hematite commonly forms irregular and pinch-and-swell shaped granules. Between granules, chamosite and muscovite occur along with microscopic grains of apatite. The chert matrix contains clay minerals and abundant carbonate rosettes. A few carbonate rosettes have sub-rhombohedral edges with circular to rhombohedral centers composed of chert and commonly contain nanoscopic hematite inclusions.

The ironstone of the Gibralter Formation is age equivalent to the Lake Superior iron formation. The maximum age of deposition comes from a detrital zircon U-Pb age of 1883 ± 10 Ma from underlying clastic sedimentary rocks of the Sosan Group (*66*), whereas the minimum age constraint was derived from ages of Compton intrusions (a mean age of 1865 ± 15 Ma; *67*), that intrude carbonate sequences of the upper Pethei Group.

The ca. 1878 Ma Sokoman Formation, Ferriman Group (Canada)

The Orosirian Ferriman Group of the Labrador Trough (Quebec, Canada) comprises the Wishart, Nimish, Ruth, Sokoman, and Menihek Formations (in ascending order) (*68*). The Sokoman Formation features a ~100 m thick succession of granular iron formation interbedded with mudstone, sandstone, and conglomerate interpreted to record deposition in a shallow shelf setting (*69, 70*). The iron isotope composition of the Sokoman Formation was documented by Raye et al. (*71*).

The Sokoman Formation ironstone is predominantly hosted by granular hematite beds and stromatolite-bearing, flaser-bedded grainstone featuring hematite intraclasts cemented by chert and iron ooids composed of alternating fine laminae of hematite and silica (*69*). Wavy- and cross-laminated, magnetitic siltstones are also present (*69*). The Sokoman Formation is mineralogically complex (*72-74*), with chert, magnetite, hematite, minnesotaite and siderite as the most common minerals (*74*). In some localities, the Sokoman Formation is more dominated by silicate-facies iron minerals, such as greenalite, stilpnomelane, minnesotaite, and crocidolite with minor siderite and ankerite (*72*). Overall, the ironstone of the Sokoman Formation is interpreted to represent deposition in nearshore and peritidal environments (above fair-weather wave base) due to the upwelling of ferruginous seawater (*69*).

The age of the Sokoman Formation is estimated to be ca. 1880 Ma, based upon the geochronology of the associated igneous rocks in the Labrador Trough. These constraints include U-Pb zircon ages of 1884.0 ± 1.6 Ma from a gabbro sill that crosscuts the Sokoman Formation, and 1877.8 ± 1.3 Ma obtained from syenite cobbles interpreted to be sourced from the Nimish Volcanics, which are intercalated with the Sokoman Formation (*75*).

The ca. 1660 Ma Freedom Formation (USA)

The Statherian Freedom Formation (Wisconsin, USA) overlies conformably the Seeley Slate that is underlain by the Baraboo Quartzite (*76*). The Freedom Formation is 300 m thick and consists of ferruginous

shales, cherts, and iron-rich dolostones. Samples for this study come from one drill core from the Gahoon Iron Mine on the southern limb of the Baraboo syncline.

The granular hematite-rich member occurs locally in the lower half of the formation. The ironstone is quartz-rich, with jasper laminae featuring hematite granules and coarse quartz grains, as well as subordinate magnetite, chlorite. Micritic dolomite cement is also common, and coarsely crystalline dolomite locally overprints precursor granules. The magnetite and hematite occur dominantly as mm-scale granules cemented by chert and jasper (*77*). In places, chamosite ooids are present in a mudstone and silt matrix.

A maximum depositional age for this unit comes from the youngest detrital zircons in the Baraboo Quartzite (1710 Ma; *78*). It has been suggested that folding of these sedimentary successions occurred at ca. 1630 Ma (*76*), which provides a minimum age of the unit. Given the above constraints, we tentatively assign an age of 1660 Ma to the Freedom Formation ironstone.

The 1650 Ma Chuanlinggou Formation, Changcheng Group (China)

The Statherian Chuanlinggou ironstone (also known as Xuanlong-type iron deposit) is part of the Changcheng Group and was deposited in the Yanshan Basin, a continental rift developed on the northern margin of the North China craton between ca. 1800 and 1600 Ma (*79*). The Changcheng Group constitutes the lowest part of the mid-Proterozoic succession of the Yanshan Basin and comprises, in stratigraphically ascending order, the Changzhougou, Chuanlinggou, Tuanshanzi, and Dahongyu formations. This group is dominated by siliciclastic sedimentary rocks with a metamorphic grade generally below prehnite-pumpellyite facies (*80*).

Samples for this study come from the Jixian area (North China). The Chuanlinggou Formation in the Jixian area consists mainly of coarse sandstones and conglomerates indicative of shallow subtidal to intertidal environments. The lower Chuanlinggou Formation represents a littoral-intertidal marine environment with ironstone, silty shale, and interbedded sandstone, which grade upwards into subtidal black shales with frequent intercalations of intertidal sandstone and dolostone. The ironstone member contains ooidal, stromatolitic, and granular facies. The iron mineralogy of the member is dominated by hematite with minor pyrite and siderite in the part of the ooidal facies (*77*). The ooidal facies contain coarse sand-sized coated grains typically interspersed with finer quartz sand grains (Fig. S5b). The iron ooids range from 0.3 mm to 4 mm in diameter and are commonly spherical to ellipsoidal with lesser amounts of ooids displaying squashed ellipsoidal and irregular dumbbell shapes. Hematite ooids exhibit concentric laminations of iron-oxide, which also occurs around quartz grains as massive cement. The stromatolitic ironstone is composed of densely packed cm-scale vertical stromatolite columns, whereas the granular facies contain medium sand-sized hematite grains lacking internal structure. Our Fe isotope data from the Chuanlinggou Formation ironstone are supplemented by data from Li and Zhu (*81*) and Lin et al. (*82*). A detailed Fe–S–C–Mo geochemical study of the Chuanlinggou Formation by Li et al. (*83*) concluded that this succession was deposited in a basin characterized by ferruginous water column conditions.

The minimum depositional age comes from the LA-ICP-MS U-Pb age of the youngest detrital zircon derived from the basal Chuanlinggou Formation (1657 ± 17 Ma; *84*), which is supported by U-Pb dating of a diabase (1638 ± 14 Ma; *85*) and a diorite porphyrite (1634 ± 9 Ma; *86*) that intrude the Chuanlinggou Formation. A LA-ICP-MS U-Pb zircon age of 1641 ± 4 Ma obtained from volcanic rocks of the overlying Tuanshanzi Formation provides a maximum age constraint on the Chuanlinggou Formation (*86*). Therefore, the Chuanlinggou ironstone is considered to have been deposited between ca. 1650-1640 Ma.

The ca. 1320 Ma Sherwin Formation, Roper Group (Australia)

The Ectasian Roper Group (Northern Territory, Australia) consists of a thick (1–5 km) succession of dominantly siliciclastic sedimentary rocks (*87, 88*). There are two contrasting tectonic models proposed for the origin of the Roper Group. One model suggests that the Roper Group strata were deposited in a shallow-marine to shelf environment that originated as an epicontinental platform in response to lithostatic extension and sagging (*89-91*). The other suggests that the Roper Group represents a ramp depositional succession that was deposited during orogenic flexure (*87*). The Roper Group is subdivided in two subgroups: the Colara and Maiwork subgroups.

The Sherwin Formation is in the Maiwok Subgroup and comprises a ~100 m thick interval of crudely bedded to trough cross-stratified sandstones, siltstones, and mudstones with ooidal ironstone lenses interpreted to have been deposited in a marginal marine setting (*92, 93*). The Sherwin Formation is in gradational contact with the underlying peritidal sediments of the Moroak Sandstone and the overlying siltstones of the Kyalla Formation, interpreted to represent storm-dominated shelf deposits (*93*). At least

four laterally discontinuous ironstone horizons (up to 8 m thick) have been identified within the Sherwin Formation (*93, 94*). These ironstone horizons typically feature massive beds of iron ooids and pisoids which are typically ~0.5–5 mm in diameter (Fig. S5c), and are interbedded with coarse-grained ferruginous (chamosite-siderite) sandstones (*93*). The iron ooids and pisoids are predominantly composed of hematite and goethite (*93*). However, in places the Sherwin ironstone is dominated by ferrous phases, and both laminated beds and ooids composed of berthierine and greenalite have been reported from drill core (*95*).

The depositional basin of Sherwin Formation has been interpreted to have featured ferruginous waters which expanded onto the shallow shelf during ironstone deposition (*95*). Studies of the Fe–S–C–Mo geochemistry of the Velkerri Formation—which is stratigraphically overlain by the Moroak Sandstone and Sherwin Formation—to show that while isolated episodes of euxinia punctuated the earlier deposition of the Roper Group, the basinal waters were either ferruginous or oxic during deposition of the upper Velkerri Formation (*96-98*)

The age of the Sherwin Formation is constrained by detrital zircon U-Pb geochronology, with a minimum age of 1313 ± 47 Ma implied from detrital zircon ages in the overlying Kyalla Formation and a maximum age of ca. 1345–1320 Ma based upon detrital zircon age populations in the underlying Moroak Sandstone (*99*). The upper Velkerri Formation, which underlies the Moroak Sandstone, has been dated to 1361 ± 21 Ma using whole-rock Re-Os geochronology (*100*). Therefore, the Sherwin Formation is estimated to have been deposited at ca. 1320 Ma.

The ca. 900 Ma Nelson Head Formation, Rae Group (Canada)

The Tonian to Cryogenian Shaler Supergroup (~1100–723 Ma) is a >4 km thick sedimentary succession composed of predominantly shallow-marine carbonate rocks interlayered with mudstones, sandstones, and sulphate deposited in the Amundsen Basin (*101*). The Shaler Supergroup consists of, in ascending order, the Rae Group, the Reynolds Point Group, and a set of ungrouped formations (*102*).

The ironstone of the Rae Group occurs as a thin sharply gradational contact zone between the Nelson Head Formation and the overlying Aok Formation (Fig. S4a). The uppermost Nelson Head Formation comprises planar and trough cross-stratified sandstones, variably featuring wavy bedding and hummocky cross stratification (*103*). This upper Nelson Head Formation interval is interpreted to have been deposited in prograding marine delta and barrier island–lagoon settings during transgression to marine conditions (*102, 103*). The Aok Formation is a ~50 m succession dominated by iron-rich (sideritic and ankeritic) dolomite composed of columnar stromatolites, interpreted to represent a marine platform environment (*102, 104, 105*). The Nelson Head ironstone is a thin (~0.5 m) interval comprised of alternating centimeter-scale beds of near-pure hematite and jasper with minor dolomite. The hematite-dominated layers are composed of hematite granules cemented by coarse hematite and microcrystalline chert (Fig. S5d).

The maximum age of the Nelson Head Formation is constrained by detrital zircon geochronology at 1013 ± 25 Ma of the underlying Nelson Head Formation (*106*). The depositional age of 892 ± 13 Ma based on Re-Os black shale geochronology in the overlying Boot Inlet Formation provides the minimum depositional age (*107*). The digitate stromatolites within the Aok Formation have been suggested to be a regional stratigraphic marker and correlative to the McClure Formation of the Katherine Group in the Mackenzie Mountains (Northwest Territories, Canada; *103, 105, 108*).

The ca. 900 Ma McClure Formation, Katherine Group (Canada)

The Tonian Katherine Group (*108*) is a ~1.5 km thick siliciclastic succession that represents the middle group of the Mackenzie Mountains Supergroup in the Mackenzie Mountains (Northwest Territories) and the Wernecke Mountains (Yukon). This package is dominated by sandstone, with subordinate siltstone and mudstone and featuring minor carbonate horizons, interpreted to have been deposited in a shallow marine setting (*108, 109*). The Katherine Group is defined and subdivided in the Mackenzie Mountains into the Eduni, Tawu, Grafe River, Etagochile, Shattered Range, McClure, and Abraham Plains formations (in stratigraphically ascending order; *108*).

The ironstone unit occurs in the upper Katherine Group in the Wernecke Mountains (Fig. S4b). Three ferruginous intervals (each < 5 m thick) were identified, featuring hematite-cemented sandstones and hematite-berthierine oncoid/pisoid-bearing ironstone with abundant well-rounded quartz grains in a mixed, fine-grained hematite-berthierine matrix. Iron oncoids and pisoids form distinctive beds and are typically nucleated around intraclastic lithic fragments of laminated hematite siltstone or pisoids (i.e. composite coated grains). The fine lamination in the pisoid/oncoid cortices is composed of hematite and

berthierine (Fig. S5e), which can be seen to be locally overprinted by coarse hematite or mottled berthierine. These oncolitic and pisolitic horizons feature ferruginous crusts, as well as desiccation cracks and fenestrae indicating wetting and drying cycles. The ferruginous horizons are predominantly interbedded with dark grey mudstones and siltstones (featuring mudcracks) and coarse, cross-bedded sandstones (featuring wave ripples). The Katherine ironstone units are overlain by thick-bedded (>2 m), massive to cross-stratified, highly mature orthoquartzites. Iron speciation data show that there is negligible pyrite in the shales and siltstones of the ca. 100 m thick sedimentary package that underlies the ironstone interval, which indicates that the water column leading up to ironstone deposition was not euxinic (Dataset S3).

This sedimentary package is tentatively correlated with the McClure Formation of the Mackenzie Mountains based on similar lithostratigraphic profiles, including the presence of characteristic stromatolites in the underlying strata. This would suggest that the ironstone occurs near the contact between the McClure and Abraham Plains formations, although the Katherine Group stratigraphy remains informally defined in the Yukon (*110*). The McClure Formation has been suggested to be directly equivalent to the Aok Formation of the Shaler Supergroup based on sequence stratigraphy and a distinct stromatolitic marker horizon (*102*). A direct minimum age is provided by the Little Dal Basalt, which occurs at the top of the overlying Little Dal Group in the Mackenzie Mountains and has been correlated geochemically with the ca. 775 Ma mafic intrusions that crosscut the overlying Little Dal Group (*111*). A significant negative carbon isotope anomaly recorded within the Rams Head Formation (Little Dal Group) has been correlated to the Bitter Springs Anomaly, a carbon isotope excursion considered to be globally contemporaneous (*112*) at ca. 811.5 Ma (*113*). In the absence of rigid geochronological constraints, and given no significant unconformities occur between the Katherine Group and the Ram Head Formation in the Mackenzie Mountains, we estimate the McClure ironstones to have been deposited ca. 900 Ma.

The ca. 750 Ma Galeros Formation, Chuar Group (USA)

The well-preserved sedimentary strata of the Tonian Chuar Group are exposed in a broad, doubly plunging syncline along several tributaries of the Colorado River in the eastern region of the Grand Canyon, Arizona. The 1600-m-thick Chuar Group is dominantly composed of organic-rich shale with subordinate meter-scale beds of sandstone and dolomite (*114, 115*). It is divided into three formations in gradational contact: the basal Nankoweap Fomation, the Galeros Formation, and the overlying Kwagunt Formation. The Galeros Formation is subdivided into the Tanner Member, Jupiter Member, Carbon Canyon Member, and the ironstone-bearing Duppa Member (Fig. S4c) (*116*). The relative abundance of different iron mineral species in the Chuar Group strata has been used to argue that the basinal conditions were dominated by ferruginous seawater (*117*). Importantly, the Chuar Group preserves diverse microfossil assemblages, including vase-shaped microfossils and acritarchs with morphologically complex ornamentation (*118, 119*).

The ironstone occurs in the Duppa Member, near the contact with the overlying Carbon Butte Member of the Kwagunt Formation (*120, 121*). The Duppa Member is ~30–180 m in thickness (*116*) and dominated by mudstone with sandstone and limestone interbeds. Sandstones featuring symmetrical ripple marks and mudcracks are common in the upper Galeros Formation: these sedimentary structures are considered to be indicative of intertidal to subtidal marine setting (*114, 122*). The dominant lithology of the Galeros ironstone is ferruginous sandstone, comprised of rounded to subangular quartz grains in a matrix of fine-grained hematite, cemented by coarse hematite crystals and silica (*116*). The Galeros ironstone features a thin (<30 cm) oolite horizon (*120*), with poorly-cemented beds of iron ooids which are typically ~500 μm in diameter and feature fine, concentric laminae of hematite with variable silica content (Fig. S5f). In places, these iron ooids appear to have undergone plastic deformation, suggesting that they were deposited as iron oxyhydroxides and deformed during sedimentation prior to lithification. The Fe–S geochemistry of the Chuar Group was investigated by Johnston et al. (*123*), who concluded that ferruginous conditions persisted in the bottom waters of the depositional basin.

A U-Pb age of 782 Ma on detrital zircons from the Nakoweap Formation provides the maximum depositional age to the Chuar Group (*115*). Zircons recovered from a tuff within the uppermost Walcott Member of the Kwagunt Formation yield a weighted mean U-Pb age of 729.0 ± 0.9 Ma, providing a minimum depositional age of the Chuar Group (*124*). A Re-Os date of 757.0 ± 6.8 Ma from organic-rich carbonates in the Carbon Canyon Member, combined with a Re-Os date of 751.0 ± 7.6 Ma from marcasite nodules in the Awatubi Member, provides both maximum and minimum ages, respectively, for the Duppa Member (Fig. S4) (*124*)

The 465 Ma Cap de la Chèvre Formation (France)

The Ordovician Cap de la Chèvre Formation of the Amorican Massif (Brittany, France) comprises ferruginous sandstones, conglomerates, and siltstones (*125*). The ironstones are 0.2–2.5 m in thickness, predominantly composed of hematite with lesser magnetite, apatite, chamosite, and minor stilpnomelane (*126*). Ironstone horizons feature concentrically laminated, hematite-coated grains (*127*). These deposits are interpreted to have been deposited in intertidal to subtidal depositional environments (*126*). The Cap de la Chèvre Formation ironstones are part of a belt of ferruginous deposits of southwestern Europe that were deposited in nearshore settings of Gondwana during the Early Ordovician (*126*). The iron enrichment is considered to be the product of oxidation of continentally-sourced Fe(II) and the precipitation of Fe oxyhydroxides in the water column, with magnetite and berthierine forming due to iron reduction during diagenesis (*126*). The age of the Cap de la Chèvre Formation is constrained by a U-Pb age of 465 ± 1 Ma from interbedded volcanoclastic rocks (*128*).

The ca. 438 Ma Birmingham ironstone, Red Mountain Formation (USA)

The Silurian Birmingham ironstone occurs in the lower part of the Red Mountain Formation of the southern Appalachian Valley and Ridge across Alabama, Georgia, and Tennessee (USA). The Red Mountain Formation is an unconformity-bounded unit including all Silurian strata, comprising the Taylor Ridge, Duck Springs, Birmingham, Ruffner, and Rocky Row Members (*129, 130*). This succession features twelve horizons of ooidal ironstones (*131*), predominantly hosted by the Birmingham Member (*130*). The biostratigraphy of the Red Mountain Formation has been used to constrain the ironstone intervals to the middle Aeronian to early Telychian stages of the Silurian Period (ca. 440–435 Ma; *130*).

The Red Mountain Formation comprises siltstones (including red-bed horizons) and hummocky cross-stratified sandstones, with ironstones hosted by ferruginous sandstones and conglomerates (*130*). Reworking is common, as evidenced by the rounded quartz grains and abrasion of skeletal fragments which are cemented by goethite (*130*). These units are interpreted to represent deposition in a high-energy, shoreface environment, accumulating as shallow marine sand bars deposited in tidal deltas or lagoonal settings (*130, 131*). The ironstones contain iron ooids, pisoids, and peloids predominantly composed of goethite and hematite coating detrital quartz grains and skeletal fragments (*130*). In some cases, cortical hematite laminae are interlaminated with chamosite (*130, 132, 133*), and chamosite ooids occur locally in offshore limestone facies (*129*). The textural and geochemical differences between the hematitic and chamositic ooids have been used to suggest that these ooids do not have a common origin, and that both represent primary ooid phases deposited under distinct water column chemistry (*134*). Our study focused only on the hematitic ooids of the Birmingham ironstone.

The ca. 433 Ma Clinton Group (USA)

The Silurian Clinton Group was deposited in the Appalachain Foreland Basin in Pennsylvania and New York (USA) following the Taconic Orogeny and prior to or coincident with the deformation of the Salinic Disturbance (*135*). The stratigraphy of the Clinton Group varies regionally: in Pennsylvania, ironstones occur in the Rose Hill Formation and the Keefer Formation (*136*). In New York, the Clinton Group can be subdivided into four unconformity-bound packages (*135*), in which ironstone intervals are hosted by the Westmoreland, Dawes, and Kirkland formations (*137, 138*). The biostratigraphy of the Clinton Group (based upon brachiopod, ostracod, and conodont assemblages) indicates that the ironstone intervals were deposited during the late Telychian to early Sheinwoodian ages (ca. 435–430 Ma; *135, 139-141*).

The ironstones feature ooidal horizons (*136, 139, 141, 142*) that are typically <0.5 m thick and associated with sandstones featuring flaser bedding, wave ripples, hummocky cross stratification, and burrows (*136*), and the ooidal beds can also be cross stratified (*141, 143*). The ironstone intervals are commonly associated with intraclast breccias featuring skeletal fragments and phosphate granules, considered to represent condensed lags reworked by storm agitation with many of the iron ooid horizons considered to have been transported (*136, 143*). *In situ* ooidal ironstones feature burrows and phosphate nodules (*136*) and are interpreted to have been deposited in shallow marine shoal settings at or above storm wave base (*136, 141, 144*). Sandstones can be hematite cemented (*144*) and iron ooids are predominantly composed of hematite and goethite laminae surrounding cores of skeletal fragments and quartz grains (*136, 141, 144-146*). However, in some cases ooids show alternating chamosite and hematite laminae (*144*). The underlying strata do not appear to be significantly depleted in iron, which has been used to argue that the ferrous iron source for ironstone genesis was not derived from a local benthic iron flux (*141*). Fossil evidence for diverse animal ecosystems and bioturbating organisms (*139*) suggests oxic

bottom water conditions (*141, 144*). However, Cotter and Link (*136*) suggested that the many of the ironstone horizons were redeposited, and the in situ horizons formed as authigenic berthierine ooids at the redoxcline in a stratified basin. Overall, the ironstones are interpreted to have formed in shallow marine settings along the margins of a redox stratified basin, near the intersection of the redoxcline with the seafloor (*136, 144*).

The 170 Ma Blaukalk ironstone, Wedelsandstein Formation (Germany)
The Wedelsandstein Formation is a ~30-meter-thick package of limestone and marl within the continuous Middle Jurassic carbonate succession of southern Germany. The Wedelsandstein Formation features the informal "Blaukalk" ironstone, a ~2-meter-thick ferruginous, fossiliferous limestone (*147*) comprising marl, calcarenite, and peloidal limestone. The ironstone-bearing interval of the Blaukalk features hematite-cemented calcarenites, and a 0.5 m horizon of abundant goethite ooids (*148*). The Blaukalk ironstone conformably overlies the fine-sandy marls of the "Oberer Wedelsandstein", which feature burrows with phosphate nodules, and is overlain by marls of the Rimsingen Ton (*148, 149*). The ammonite biostratigraphy of the Wedelsandstein Formation places the Blaukalk ironstone in the Sauzei Zone of the Bajocian Stage (*148*).

The ca. 163 Ma Villers Formation (France)
The Villers Formation is located in Villers-sur-Mer (Normandy, France) and consists of about 5 m of micritic limestone intercalated with marl (*150*) deposited under shallow marine conditions. The unit is also bioturbated and features abundant fossil corals, gastropods, and ammonites. The Villers Formation ironstone features goethite ooids and calcite ooids considered to have replaced iron oxides during diagenesis (*2*). In places, the goethitic ooids feature encrusting foraminifera within ooid laminae (*151*), indicating a syndepositional marine origin. The ammonite biostratigraphy of this unit indicates a Lower Oxfordian age (*152*).

The ca. 120 Ma Hidra Formation, Galilee Group (Israel)
The Hidra Formation of the Galilee and Golan regions (northern Israel) consists of sandstone, iron ooids within a fossiliferous limestone, and marl (*153, 154*). Our samples were collected from the upper part of the Hidra Formation composed of limestone rich in marine fossils, siliciclastics, and goethite ooids. The laminated, cross-bedded or bioturbated sandstones and siltstones rocks suggest a shallow subtidal to outer platform environment (*155*). An Aptian age has been assigned based upon ostracod biostratigraphy (*156*).

The ca. 110 Ma Hatira Formation (Israel)
The strata of the Hatira Formation (*157*) is a mixed carbonate-siliciclastic succession in the Negev, southern Israel. This unit is predominantly composed of sandstones and interpreted as fluvial and shoreface marine deposits (*158*) interbedded with limestone, dolomite, and marl interpreted to represent shallow marine deposition (*156*). These marine carbonates contain goethitic and hematitic ooids. The ammonite biostratigraphy of the Hatira Formation indicates an Albian age for the ironstone horizons (*2*).

The ca. 87 Ma Bad Heart Formation, Smoky Group (Canada)
The Bad Heart Formation is an ironstone-bearing, siliciclastic unit within the Late Cretaceous Smoky Group of northwest Alberta (Canada; *159*). Typically ranging from 5 to 15 m thick, the Bad Heart Formation is characterized by sandstone with ooidal sandstone, and siltstone with thin, discontinuous conglomerate lenses (*159*). The Bad Heart Formation overlies a regional unconformity interpreted to represent subaerial uplift, with the ironstone-bearing intervals occurring in the middle of the succession within sandstone packages (*159*), considered to have been deposited under high-energy, shallow marine conditions above wave base (*160, 161*). The mineralogy of the ooids is dominated by goethite and nontronite laminae around detrital fragment cores, including quartz, feldspar, and ooid fragments (*161*). These iron ooids are interpreted to have formed on the seafloor in a high-energy marine environment, with locally Fe(II)-rich conditions due to hydrothermal activity associated with nearby fault systems (*161*). The Bad Heart ironstone has been assigned a middle to late Coniacian age based upon ammonite biostratigraphy (*162, 163*).

The ca. 59 Ma Bakchar ironstone, Lyulinvor Formation (Russia)
The Paleocene Lyulinvor Formation (West Siberian Basin, Russia) hosts several ironstone horizons (*164*). This formation is characterized by ooidal ironstones, sandstones, and siltstones interpreted to represent

shallow marine shoreface deposits (*165*). The Bakchar ironstone occurs at the bottom of the Lyulinvor Formation and is composed of two facies: uncemented (loose) and siderite-cemented ooidal ironstones. Our samples come from the Bakchar ironstone, which occurs at the bottom of the Lyulinvor Formation and features goethitic ooids with minor chamosite. The palynology of the Lyulinvor Formation constraints the depositional age of the Bakchar ironstones to the late Paleocene, ranging from ca. 56 to 62 Ma (*166, 167*).

Origin of ironstones.

Depositional Environment

Ironstones feature a characteristic stratigraphic association with deltaic to shoreface sandstones and peritidal mudstones, featuring flaser bedding and dessication cracks. These sandstones may feature planar, trough, or hummocky cross stratification, intraclasts, and other evidence for sediment reworking. Less commonly, ironstones are associated with shallow marine carbonates featuring stromatolites, intraclasts, and mud drapes. As such, ironstones are near-exclusively interpreted to have been deposited in shallow marine environments, with estuarine, peritidal, lagoonal, shoreface, and shelf settings above storm wave base variously proposed for ironstone deposition (*132, 151, 168-179*). Where present, body fossil and ichnofossil assemblages of ironstones also indicate a shallow marine depositional setting (*141, 144, 180*). In some rare cases, ironstone Fe ooids are interpreted to have been reworked from shallow settings and resedimented in deeper marine environments during storm surges (*1, 181*). All of the ironstones analyzed for this study are interpreted to have been deposited in nearshore marine settings.

The tumbling of Fe ooids by water column agitation has historically been believed to be important for iron ooid genesis (*182-184*). Well-rounded grains commonly forming the cores of iron ooids also likely require abrasion by wave action (*181, 185*). However, irregular cortical structures in Fe oncoids and pisoids (*175, 186*), have been suggested to imply a biological influence on their growth (*187, 188*). Multi-directional growth patterns in the rims of Fe oncoids have also been compared to microstromatolites and interpreted as and evidence for the rolling of Fe coated grains by wave action (*181*). Alternatively, some Phanerozoic iron ooids have been suggested to have formed *in situ* near the sediment–seawater interface due to Fe mineral precipitation from Fe(II)-bearing porewaters during early diagenesis (*170, 171, 179, 189, 190*).

There is evidence for synsedimentary Fe ooid formation during extensive reworking, as indicated by multiple generations of ooid formation (i.e. composite ooids with nucleation on brecciated ooid fragments) and cross-stratified Fe ooid beds (*191*). Fossils of encrusting benthos such as foraminifera, bryzoans, and serpulids within Fe ooid laminae have been documented in several ironstones (*151, 174, 186, 192*). These features require that ooid formation took place either in the water column, on the seafloor, or close enough to the sediment–seawater interface to facilitate frequent reworking by storm currents. Iron ooids often feature rounded quartz grains trapped within the ooid cortices, with matrix grain-size changes delineating the boundaries of the iron ooids, indicating that the at least some of the Fe ooids were deposited as a discrete sedimentary granule rather than concretion.

In summary, ironstones are generally considered to have deposited in shallow marine environments with at least intermittent high energy (in water depths close to, or above, storm, and fair-weather wave base) (*1, 176, 188, 193-195*). We suggest that the authigenic ironstone Fe(III) (oxyhydr)oxide minerals, and potentially some of the ferrous clays, formed due to direct precipitation at the sediment–seawater interface.

Iron Mineralogy Paragenesis

The mineralogy of ooidal ironstones typically falls into two categories: those dominated by Fe(III) (oxyhydr)oxides (typically goethite or hematite) or Fe(II) silicates (typically chamosite or berthierine). Siderite, pyrite, and glauconite are also reported in lower abundance (*171, 196-198*). These minerals can form the nucleus or cortices of coated grains, and commonly also occur as pore-filling cement (*172*). The granules can be either grain-supported, matrix-supported or cemented (*199*). In places, some Fe(III) oxides appear to be the product of post-depositional oxidation of Fe(II)-bearing clays (*198, 200, 201*), and the overprinting of precursor phases by berthierine or chamosite is also observed (*202, 203*). However, in many ironstones there is convincing evidence for a primary origin for ferric oxyhydroxides (*132, 174, 179, 182, 198, 202*), and many ironstone ferrous clays also appear to be either primary seafloor precipitates or formed from porewater during early diagenesis (*95, 179, 200, 204-206*). An authigenic, synsedimentary origin for both ferric and ferrous phases is clearly evident in ironstones which feature Fe ooids with interlaminated goethite/hematite and berthierine cortical laminae (*134, 186, 207*), which suggests at least some ironstones formed at the redox boundary between Fe(III) and Fe(II) throughout their deposition.

For this study, we focused on ironstone samples predominantly composed of Fe(III) (oxyhydr)oxides interpreted to be primary precipitates, and late-stage replacement products were avoided during Fe isotope analysis. Based on the preservation of fine lamination in the Fe(III) (oxyhydr)oxide ooids of many of these ironstones, and the absence of evidence for recrystallization or replacement textures, we suggest that the hematite and geothite of these ironstones represent primary, synsedimentary phases. This is supported by the positive δ^{56}Fe values of the ironstones, as the authigenesis of Fe(II) phases from aqueous Fe(II) is expected to lead to unfractionated or negative δ^{56}Fe values (*208*). In some cases, the ironstone mineral assemblages contain berthierine (or its alteration product chamosite) which originated during early diagenesis. Rare siderite and pyrite are interpreted to be later-stage diagenetic products.

Iron source

The deep oceans are considered to have been anoxic and ferruginous throughout the Proterozoic and early Phanerozoic (*209-212*), with an oceanic Fe(II) reservoir strongly influenced by hydrothermal venting (*209, 213*). Geochemical studies of Proterozoic ironstone-bearing sedimentary successions consistently indicate that the basinal chemistry was characterized by ferruginous conditions without euxinia (*83, 95, 123*). Episodes of ferruginous deep marine conditions are also considered to have punctuated the later Phanerozoic during ocean anoxic events (*214, 215*), which would have facilitated the accumulation of seawater Fe(II) during these times. Ferruginous seawater has been proposed as a key Fe(II) source for at least some of the ironstone deposits (either through upwelling or deposition at a stratified redoxcline) from the Proterozoic (*82, 95, 175, 176*) through to the Phanerozoic (*136, 179, 196, 205, 216-219*), as well as Quaternary Fe ooids (*220*). Many ironstones are also associated with features such as organic-rich mudstones and phosphates, characteristic of oxygen-depleted seawater and coastal upwelling systems, respectively (*95, 179, 191, 216*).

Continental Fe is another source invoked for the formation of ironstones (*1, 221*). Continental Fe can be transported to marine environments primarily in the form of nanoparticulate Fe(III) (oxyhydr)oxides (*222, 223*). Stabilized in suspension in colloidal form by organic ligands, much of the riverine nanoparticulate Fe in river waters is removed from suspension due to flocculation upon mixing with saline waters in estuaries (*223, 224*), with a portion of this Fe being resuspended and transported distally (*222*). The delivery of continental Fe to shallow marine settings could have been enhanced due to lateritic weathering (*178, 188, 192*), and many ironstones are interpreted to have been deposited at tropical latitudes during greenhouse climates (e.g., *1, 177*). The reworking of continental Fe(III) (oxyhydr)oxides deposited in estuarine settings has been suggested to have led to the formation of goethite ooids in some Phanerozoic ironstones (*206*). However, given that the Fe ooids of ironstones appear to be authigenic precipitates, most ironstone models require any continental Fe(III) to be remobilized by reduction to Fe(II) (*225*). The reductive dissolution of Fe(III)-bearing minerals coupled to organic matter respiration (dissimilatory iron reduction; DIR) provides a flux of Fe(II) from the seafloor of dysoxic continental shelves (*226-228*) which can be exported to the oceans and upwelled to surface waters (*229, 230*). Continental Fe can also be exported to seawater via the nonreductive release of Fe-bearing minerals, a process which is documented from the modern, oxic seafloor of continental margin sediments (*231*), and is considered to provide a significant proportion of the Fe flux to the modern oceans (*232*). In sum, both seawater enriched in hydrothermal Fe(II) and a benthic flux of Fe(II) sourced from the redox cycling of continentally sourced Fe could have contributed to ironstone genesis.

Possible mechanisms for Fe isotope variability.

Detrital iron contribution

The potential Fe isotope compositions of Fe(II) sources to the ancient ocean are well constrained. The mass-weighted bulk detritus from riverine fluxes are close to those of the average of igneous rocks (~0 ‰) (*233*). Because of the abundance of Fe in ironstones (typically > 15 wt% Fe) compared to that of common detrital materials (e.g. ~3.5 wt% Fe for upper continental crust; *234*), ironstones are strongly rock-buffered with respect to their Fe isotope composition. Therefore, a high degree of detrital contamination is required in order to mask the authigenic Fe isotope signature of ironstones.

In order to investigate the possible detrital contribution to the Fe isotope composition of the studied ironstones, we use immobile elements such as Al and Ti as geochemical proxies for detrital contamination. Although we targeted ironstones dominated by primary Fe oxide ooids, the elevated Al contents within some of the samples are likely due to the presence of authigenic Fe-rich aluminosilicates (such as berthierine and chamosite). Therefore, while high Fe/Al ratios are a robust proxy for insignificant detrital

input, and high detrital input would have low Fe/Al ratios, comparatively low Fe/Al ratios (compared to Fe oxide-rich ironstones) does not necessarily require high detrital contamination. Regardless of the presence of authigenic clays in some samples, the lack of a correlation between δ^{56}Fe and Fe/Al ratios of our samples (Fig. S6) and a large deviation in δ^{56}Fe values from 0 ‰ for Proterozoic ironstones suggest that detrital materials played a negligible role in controlling iron isotopic compositions. Therefore, it is unlikely that the small degree of fractionation observed in the Tonian Galeros Formation and Phanerozoic ironstones is due to dilution of a fractionated iron isotope signal by detrital iron.

Variations in primary mineralogy

The overall Fe isotope fractionation involved in the precipitation of Fe minerals from dissolved Fe(II) is variable depending on the mineralogy of the primary precipitate (*208, 235, 236*). The primary mineralogy of ooidal ironstones has been variably interpreted to be Fe(III)-oxides such as ferrihydrite (converted to hematite during early diagenesis) or goethite (*132, 174, 179, 182, 198, 202*) and Fe(II)-silicates such as berthierine (*95, 179, 200, 204-206*). As discussed above, we suggest that the synsedimentary to early diagenetic formation of ferric (oxhydr)oxides (primarily ferrihydrite) and ferrous clays (primarily berthierine) all contributed to the genesis of ironstones to some degree. The fractionation factor between aqueous Fe(II) and ferrous clays such as berthierine is generally considered small (*208*), and the original δ^{56}Fe values of authigenic ferrous phases are expected to be close to that of the source dissolved Fe(II) (expected to be ~0 ‰). Even if these ferrous minerals are subsequently oxidized to ferric oxides, because this alteration necessarily takes place under oxidizing conditions in which Fe mobility is low (*237*), the resultant ferric oxides are also unlikely to be fractionated. Therefore, the commonly positive δ^{56}Fe values of the Proterozoic ironstones support the interpretation that ferric (oxyhydr)oxides were an important, primary phase for ironstones. We selected samples dominated by oxide-facies ironstone in order to target primary phases directly precipitated due to seawater Fe(II) oxidation. Therefore, an abundance of ferrous clays is not responsible for the lower δ^{56}Fe values of the Phanerozoic ironstones.

The Phanerozoic ironstone samples are more dominated by goethite compared to the Proterozoic samples, which are predominantly hematite: this secular shift in ironstone mineralogy has been suggested to be related to the evolution of seawater chemistry (*2*). The precipitation of goethite from aqueous Fe(II) has a lower equilibrium fractionation factor (up to ~1.2‰; *238*) than the precipitation of ferrihydrite (up to ~3‰; *235*). However, our study shows that examples of ironstone samples composed of hematite (such as the ca. 750 Ma Galeros Formation) and those composed of goethite (such as the ca. 465 Ma Cap de la Chèvre Formation) can have similarly unfractionated δ^{56}Fe values. Therefore, we suggest that the simplest explanation is that the Fe isotope variability observed in our studied samples reflect a primary feature of Fe(III)-oxyhydroxide precipitates due to a shift from partial to quantitative Fe(II) oxidation in the late Proterozoic.

Iron source isotopic composition

As discussed above, ironstones are considered to require the availability of abundant, aqueous Fe(II) for their genesis. Although the origin of this Fe(II) source continues to be debated, most researchers favor one of two main sources: ferruginous seawater enriched in hydrothermal Fe(II), and/or a benthic flux of Fe(II) produced by the reduction of continentally sourced Fe(III). The iron isotope composition of hydrothermal Fe(II) is generally accepted to have remained constant throughout geological time (*233*), with δ^{56}Fe values mostly ranging between -0.5 and 0 ‰ (*239-242*). Aerosols, loess and igneous rocks have average δ^{56}Fe values indistinguishable from crustal and igneous values (*239, 243*). Riverine Fe(III) has highly variable δ^{56}Fe values, yet bulk riverine δ^{56}Fe values cluster around 0 ‰ (*208*). Therefore, because partial Fe(III) reduction tends to preferentially release light Fe, the Fe(II) sourced from the reduction of this continental Fe(III) has variably negative δ^{56}Fe values (*244-247*). Therefore, there are no significant sources of Fe(II) supplied to seawater that have a clearly positive δ^{56}Fe signature (*236*).

Fractionation due to ligand complexation

Despite average marine particulate Fe having Fe isotope characteristics similar to crustal values in modern oceans (*248*), positive δ^{56}Fe values can be detected in dissolved and nanoparticulate Fe. Iron in the well-oxygenated modern oceans is dominantly nanoparticulate Fe stabilized in oxic seawater by organic ligands (*249*), and this process can also lead to the (nonreductive) dissolution and release of Fe from coastal sediments (*250*). Experimental observations show that ligand-stabilized, nanoparticulate Fe(III) complexes can have δ^{56}Fe values approximately 0.4–0.6 ‰ greater than the precursor Fe(III) oxyhydroxide (*251, 252*).

As such, processes related to organic ligand complexation may explain positive $\delta^{56}Fe$ values of riverine nanoparticulate Fe(III) with abundant organic matter (*253-256*), and of Fe in oceanic surface waters interpreted to be sourced from nonreductive dissolution of coastal sediments (*231, 250, 257*). A fraction of modern hydrothermal Fe can also be stabilized in solution by organic ligands and transported distally from the hydrothermal vent systems (*258, 259*), and isotopically heavy Fe ($\delta^{56}Fe < 0.3$ ‰) is documented in the surface waters of the redox-stratified Baltic Sea (*260*) which may be related to similar Fe-ligand fractionation (*208*). The overall fractionation by nonreductive dissolution of Fe is estimated to produce dissolved Fe with $\delta^{56}Fe$ values approximately 0.2 ‰ greater than the original Fe in coastal sediments (*250, 257*). So far positively fractionated Fe isotope signatures have not been documented in nearby sediments (*250*). The preferential removal of light Fe from seawater by phytoplankton uptake (as labile Fe) has also been proposed as a mechanism to fractionate seawater Fe, with studies estimating that this process could lead to an isotopically heavy Fe residue with $\delta^{56}Fe$ values enriched by up to approximately 0.1–0.4 ‰ (*248, 257, 261*).

These isotopic effects are small compared to the fractionations associated with redox transformations, and much of these nanoparticulate Fe–ligand complexes would be Fe(III) oxyhydroxides that are unavailable for incorporation into authigenic ironstone phases without subsequent Fe redox cycling. This fractionation via the preferential removal of isotopically light Fe (either as particulate rainout or phytoplankton uptake) also requires that isotopically heavy Fe is stabilized in suspension. Therefore, we argue that this phenomenon is unlikely to have exerted a strong influence on the Fe isotope systematics of ironstones.

Benthic flux from sedimentary Fe reduction

Anaerobic, microbial organisms can use Fe(III)-bearing minerals as an electron acceptor coupled to the oxidation of organic matter (known as dissimilatory iron reduction; DIR) and/or H_2 (*262*). This metabolism is common in modern anoxic sediments where organic matter is oxidized during diagenesis (*263, 264*). Considered to be amongst the oldest metabolisms on Earth (*265*), DIR was likely a major driver of iron cycling between sediments and the ferruginous oceans of the Proterozoic (*266, 267*). The reduction of Fe(III)-bearing minerals by DIR produces Fe(II) with variably depleted $\delta^{56}Fe$ values in the generated aqueous Fe(II), with fractionations of up to 3 ‰ (*244-247*). The partial reduction of Fe(III) with $\delta^{56}Fe$ values close to 0 ‰—such as volcanic, hydrothermal, or lithogenic sources or Fe(III) oxyhydroxides produced from quantitative water column oxidation—typically produces Fe(II) with negative $\delta^{56}Fe$ values (*244-247*). The degree of fractionation depends on the extent of reduction and the flux of Fe(II) produced, whereby quantitative reduction necessarily can produce an Fe(II) pool with an Fe isotopic signature inherited from the original Fe(III). Highly reactive ferric species (such as ferrihydrite and Fe-Sil gel) readily undergo a high extent of reduction in ferruginous seawater when organic carbon is available (*268*). The bacterial species facilitating DIR exerts only a minor influence on this fractionation (*208*).

The preferential dissolution and release of light Fe(II) by DIR can leave the remaining Fe(III) minerals enriched in ^{56}Fe. Numerical modelling has been used to argue that the maximum net change in bulk rock $\delta^{56}Fe$ values resulting from diagenetic Fe cycling is likely less than 1 ‰ (*269*). While this mechanism may hypothetically explain positive $\delta^{56}Fe$ values of sedimentary rocks with low authigenic Fe enrichment (*270*), this process is unlikely to significantly affect the bulk Fe isotope composition of rocks where Fe is the dominant geochemical component. Further, much of the Fe(II) produced by DIR is taken up by Fe mineral authigenesis in the sedimentary pile (*271, 272*). Given that the mineralogy of our samples is characterized by large amounts of Fe(III) (oxyhydr)oxides, and the flux of reactive Fe oxides would have been greater than the input of organic matter, it is unlikely that Fe(II) loss from DIR of authigenic ironstone minerals has greatly affected the Fe isotope composition of the studied ironstones.

The degree to which Fe(II) export by DIR can influence basinal Fe(II) isotopic compositions depends upon a number of factors, including bottom water redox conditions, sedimentation rates, and the extent of reduction (*268*). Because rates of DIR are considered to be inversely proportional to bottom water O_2 contents (*226, 227*), in basins with anoxic bottom waters, DIR can lead to a significant flux of isotopically light Fe(II) to seawater (*268*). This can subsequently lead to low $\delta^{56}Fe$ values in authigenic Fe(II) minerals, or Fe(III) oxides that result from near-quantitative oxidation (*233*). As such, DIR-sourced Fe(II) has been invoked to explain the negative $\delta^{56}Fe$ values of sediments deposited during Phanerozoic oceanic anoxic events (*273*), and Archean–Paleoproterozoic iron formations (*267, 274*). Strongly negative $\delta^{56}Fe$ values are absent in all ironstones with the exception of the Chuanlinggou Formation (Fig. 2). This may suggest that DIR was not the major Fe(II) source to ironstones. However, DIR could have been near-quantitative,

producing Fe(II) with only small fractionation. Alternatively, iron cycling involving partial Fe(II) oxidation can hypothetically offset the negative fractionation of DIR and result in the formation of Fe minerals with non-negative δ^{56}Fe values. Regardless of the role that DIR played in ironstone genesis, it is difficult to account for the positive δ^{56}Fe values of the Proterozoic ironstones without invoking partial Fe(II) oxidation.

Isotopic distillation due to partial Fe(II) oxidation

An Fe(II) reservoir can experience progressive fractionation as a result of distillation due to extensive Fe(II) oxidation, as evidenced by negative δ^{56}Fe values observed where ferruginous groundwaters mix with oxygenated seawater in coastal aquifers (*275*). The negative δ^{56}Fe values of some Archean–Paleoproterozoic iron formations have been hypothesized to have resulted from Rayleigh-type fractionation during partial oxidation of the Fe(II) reservoir, producing a dissolved residue depleted in heavy Fe isotopes (*276, 277*). Therefore, secular shifts in the Fe isotope characteristics of the seawater Fe(II) reservoir could hypothetically affect the Fe isotope composition of ironstones.

Ironstones with negative seawater δ^{56}Fe values could form through near-quantitative oxidation of isotopically depleted seawater Fe(II) due to distillation processes. Our record shows that ironstones are typically characterized by either positive or crustal δ^{56}Fe values, however, some highly negative δ^{56}Fe values are present within the Chuanlinggou ironstone. There exists an important negative correlation between Mn/Fe ratios and the δ^{56}Fe values in the Chuanlinggou ironstone (Fig. 3), strongly supporting this interpretation. Specifically, upwelling and the partial oxidation of deep water Fe(II) would cause the continuous depletion of heavy Fe isotopes in the remaining Fe(II) reservoir until negative δ^{56}Fe values can be transferred to the most proximal, nearshore settings. Higher O_2 levels in these setting could have led to the precipitation of Mn oxides, and associated quantitative Fe(II) oxidation could have led to negative δ^{56}Fe values in ironstones (*278*). Importantly, this model requires partial Fe(II) oxidation, which is consistent with the predominance of positive δ^{56}Fe values. This is indicative of a high dissolved Fe(II) to O_2 ratio of the contemporaneous shallow seawater and, by extension, a low O_2 atmosphere.

Biological Fe(II) oxidation

In addition to the indirect biological contribution to Fe(II) oxidation through the production of O_2 by oxygenic photosynthesis, there are several different microbial processes that can more directly oxidise Fe(II). Autotrophic Fe(II) oxidation can be coupled to either nitrate reduction under anoxic conditions (*279*), or O_2 reduction under dysoxic to suboxic conditions (*59, 280, 281*). Phototrophic Fe(II) oxidation can occur via anoxygenic photosynthesis (photoferrotrophy) (*282*). Under oxic, low pH conditions, acidiophilic autotrophs can also facilitate the oxidation of Fe(II) (*283*). The intracellular fixation of Fe-rich granules by photosynthetic diatoms has also been documented in modern acid mine drainage environments (*284*); analogous acidophilic photosynthesizers have been invoked to explain iron formations in the Neoproterozoic (*285*), although it remains unclear whether similar diatoms existed in Proterozoic oceans. Because both photoferrotrophs and microaerophilic Fe(II) oxidizing chemotrophs likely played a larger role in the low O_2 oceans of the Precambrian than in the modern oceans (*59, 286-288*), it is necessary to consider the possible influence that biological Fe(II) oxidation may have had on the genesis and Fe isotope composition of ironstones.

In oxic seawater at circumneutral pH, Fe(II) oxidation by O_2 is rapid (*289*), essentially limiting Fe(II) oxidizing bacteria to dysoxic to anoxic environments where biological Fe(II) oxidation can compete (*290, 291*). Prior to the advent of oxygenic photosynthesis, photoferrotrophs were likely to have been active in the anoxic surface waters (*12, 292*). Following the oxygenation of the atmosphere and surface waters in the early Proterozoic, photoferrotrophs are hypothesized to have shifted to the redoxcline of the stratified oceans where light and Fe(II) were more readily available (*60, 292-294*). Similarly, microaerophilic chemotrophs are generally envisaged to have been active near the redoxcline where Fe(II) and O_2 coexist (*286, 295*). Therefore, while they are speculated to have contributed Fe(III) oxyhydroxides to offshore marine sediments, including many Archean–Paleoproterozoic iron formations (*12, 60, 287*), photoferrotrophs and microaerophilic Fe(II) oxidizing bacteria are not generally considered to have played a major role in shallow seawater where ironstone deposition was taking place. However, the range of O_2 levels at which Fe(II) oxidizing bacteria can contribute to a significant fraction of total Fe(II) oxidation in seawater is not well-known (*286, 288, 296*). This is particularly true for photoferrotrophs, which are metabolically flexible, and only a few strains have been isolated from marine environments (*297*), with only one pelagic example (*288, 298*). Microaerophilic Fe(II) oxidizing bacteria have been shown to effectively outcompete abiotic oxidation at O_2 levels below approximately 50 μM (*286, 290*). Therefore, biological Fe(II)

oxidation likely contributed to ironstone genesis during the Proterozoic, a suggestion put forward by previous researchers (*82, 299, 300*).

The Fe isotope fractionation associated with biological Fe(II) oxidation has been measured experimentally for the oxidation of Fe(II) mediated by O_2 in the presence of cyanobacteria (*301*), photoferrotrophs (*302, 303*), nitrate-reducing chemotrophs (*304*), and acidophilic aerobes (*305*). Importantly, in all cases, the Fe isotopic fractionation was similar to that of abiotic Fe(II) oxidation of Fe(II) by O_2: the produced Fe(III) oxyhydroxides have heavier δ^{56}Fe values than the initial Fe(II) by about 1–3 ‰. This is considered to be the sum of equilibrium fractionation effect between aqueous Fe(II) and aqueous Fe(III), and a kinetic fractionation associated with the precipitation of solid Fe(III) oxyhydroxides from aqueous Fe(III) (*208*). Under suboxic conditions, the Fe(II) oxidation rate of microaerophilic Fe(II) oxidizing bacteria can outcompete that of abiotic Fe(II) oxidation (*286, 290, 291*). This implies that if biological Fe(II) oxidation played a role in the precipitation of the Fe(III)-bearing phases of ironstones, then our estimates for shallow seawater O_2 contents may be conservatively high. Therefore, although Fe isotope systematics cannot directly constrain a biological influence on ironstone genesis, when combined with a kinetic Fe(II) oxidation model, they provide a maximum constraint on shallow seawater O_2.

In sum, we suggest that the simplest explanation for the genesis of Proterozoic ironstone Fe(III) oxides—and their associated Fe isotope signatures—is the partial oxidation of Fe(II) by O_2. This reaction could have been abiotic or facilitated by microaerophilic Fe(II) oxidizing bacteria, but in either case atmospheric pO_2 is required to be below 1 % PAL.

Isotope fractionation due to pyrite formation

Kinetic isotope effects associated with pyrite formation can lead to large fractionations when the availability of H_2S is the limiting factor (i.e., sulfide-limited conditions), producing isotopically light pyrite (*306*). In the modern Black Sea, euxinic basinal waters feature dissolved iron with positive δ^{56}Fe values (*307*). Because H_2S is abundant, pyrite formation is quantitative, resulting in very low (nanomolar) Fe concentrations at depth (below ~200 m) (*307*), and the pyrite produced reflects the isotopic signature of its Fe(II) source (*308*). As such, the isotopically heavy dissolved Fe from deep waters is not transferred across the redoxcline, and shallow seawater is characterized by negative δ^{56}Fe values due to iron reduction in shelf sediments (*307*).

These Black Sea Fe–S systematics have been suggested as an analog for Proterozoic basins following the Great Oxidation Event, when increased sulfate delivery could have led to the expansion of euxinic conditions along productive continental margins (e.g., Lyons et al. 2014 Nature 506). Where present, these euxinic “wedges” could have been supplied with dissolved iron either from a benthic shuttle or from upwelling ferruginous deep waters, and this would have reacted with H_2S to form pyrite in euxinic waters. If Fe(II) was in excess of H_2S then only a fraction of the iron would have been drawn down, leading to minor fractionation of the marine Fe(II) reservoir, but negative δ^{56}Fe values in pyrite associated with partial pyrite formation (*306*). This mechanism has been suggested to have contributed to the strongly negative δ^{56}Fe values of pyrite in sedimentary rocks deposited prior to the Great Oxidation Event (*306, 307, 309*). If H_2S was in excess of Fe(II), then the Fe(II) would have been quantitatively removed as pyrite (producing sedimentary pyrite that largely matches the δ^{56}Fe values of its iron source), and this process would not affect the isotopic composition of nearshore sediments.

For sedimentary pyrite from the middle Proterozoic, δ^{56}Fe values appear to be much less fractionated compared to pre-Great Oxidation Event examples, and negative δ^{56}Fe values are rare to absent (Fig. S6). It has been suggested that pyrite formation would not have been sulfide-limited in euxinic water masses following the Great Oxidation Event (*307*), which may be supported by the pyrite Fe isotope record. Thus, pyrite formation in euxinic waters is unlikely to have significantly impacted the depositional basins of the studied ironstones.

Fractionation associated with the precipitation of iron sulfides has also been documented in hydrothermal systems. In basalt-hosted hydrothermal systems, the precipitation and settling out of isotopically light iron sulfides can result in hydrothermal plumes with comparatively heavy δ56Fe values relative to the initial vent fluid (Bennett et al. 2009 GCA 73). However, this does not lead to positive δ56Fe values in hydrothermal vent fluids (e.g., Rouxel et al. 2008 Chem. Geology 252).

Post-depositional Fe cycling

In modern systems with Fe(II)-rich groundwater sourced from dissolving Fe silicates, Fe(II) oxidation by an influx of oxygenated porewaters can produce fractionated Fe oxides ($-1 < \delta56Fe < 1$ ‰; *310*) in fractured

granite. This variability is likely related to Fe isotopic fractionations associated with transformations between Fe(II) and Fe(III) (*208*). Similarly, Rouxel et al. (*275*) show that the oxidation of ferruginous groundwater systems can produce Fe oxides with positively fractionated δ^{56}Fe values. However, both of these processes only produce scattered amorphous and well-crystalline fine-grained Fe oxides rather than Fe ooids (*275, 310*) and it also remains unclear whether multiply coated grains similar to those observed in ironstones could be generated under these conditions. Furthermore, intensive Fe redox cycling across a density interface between anoxic groundwater and O_2-deficient porewaters commonly generates a large range of δ^{56}Fe values (from -2 to 1.5 ‰) in newly formed Fe oxides (*311, 312*). However, such a large-scale Fe isotope fractionation and highly negative δ^{56}Fe values are not observed in Proterozoic ironstones. Crucially, the largely unfractionated Fe isotope compositions of those Phanerozoic ironstones show that positive δ^{56}Fe values are not inherent to ironstone genesis. Therefore, we suggest that the most likely explanation for the observed secular trend of the iron isotope composition in ironstones is a shift in shallow marine redox state related to a rise in atmospheric O_2.

Hydrothermal alteration and metamorphic overprint

Iron-rich rocks such as ironstones and iron formations are considered to be resistant to the overprinting of their Fe isotope signatures by hydrothermal and metamorphic processes (*313*) and therefore robust archives of Fe isotope signatures. High temperature processes do not tend to lead to strong fractionations in the Fe isotope system (*208*). Hydrothermal fluids generally have δ^{56}Fe values ranging between -0.5 and 0 ‰ (*239-242*), and therefore hydrothermal overprinting can only drive ironstone δ^{56}Fe toward these values. There is no evidence for a strong hydrothermal overprint on the distribution of Fe in the studied ironstones, with fine-scale textures and sedimentary structures well preserved and a lack of recrystallisation, fractures, and veins. The near-absence of positive Eu anomalies—an index of high-temperature hydrothermal fluids (*314*)—in the analyzed ironstone samples (Data S2) is not supportive of the hydrothermal overprinting Phanerozoic samples.

Some Proterozoic iron formations and ironstones have experienced low-grade metamorphism, by which process the Fe isotopes may be redistributed by either diffusion or by mineral reactions. Diffusional rates and spatial scales suggest that the primary millimeter- and micrometer-scale Fe isotope heterogeneity that may have resulted from either the deposition or early diagenesis of Fe-rich sediments (*315*) might be erased by the effects of regional metamorphism (*12, 316*). However, the bulk Fe isotope compositions are expected to still be reflective of those of the original Fe-rich sediments. Dauphas et al. (*317, 318*) reported generally positive iron isotope data for high-grade (up to granulite facies) banded rocks from Greenland and Canada, and interpreted these values as a consequence of low-temperature processes involving transport, oxidation, and precipitation of Fe, suggesting that metamorphism did not affect the bulk Fe isotope compositions. Frost et al. (*319*) concluded that the isotopic compositions of the ca. 1880 Ma Biwabik iron formation magnetite were not changed during contact metamorphism relative to their pre-metamorphic compositions. By contrast, Valaas-Hyslop et al. (*320*) argued that δ^{56}Fe values in metamorphic Biwabik iron formation were 0.3 ‰ lower than those in their protolith and concluded that metamorphism decreases the δ^{56}Fe values in rocks containing iron silicates. In either case, positive δ^{56}Fe values cannot be explained by metamorphic reactions. The pristine preservation of fine-scale lamination and textures within the Fe-ooids of the studied ironstones argues against the influence of texturally destructive metamorphism. Given that only a few studied samples have experienced low-grade metamorphism, we can be reasonably confident that Fe isotopic compositions are likely to be primary in nature.

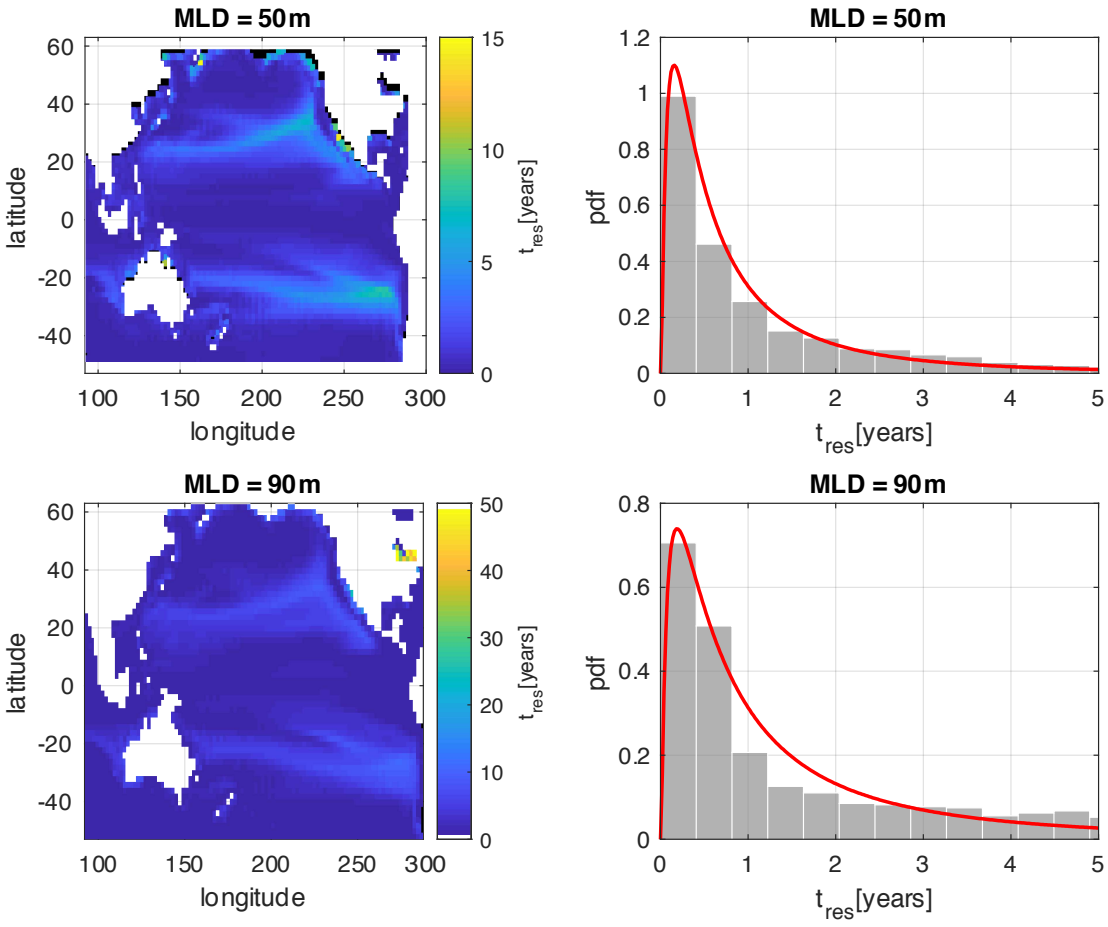

Fig. S1.

Water parcel residence times in the mixed layer for a high-resolution general circulation model (results from *9*). Results are shown for two assumed mixed layer depths, 50 m (top) and 90 m (bottom). Spatial distributions of water parcel residence times are shown on the left, while the distributions (grey bars) and the lognormal fits implemented in our model (red curves) are shown on the right. Each iteration of our stochastic routine resamples randomly from the fitted lognormal distributions to provide an oxidation timescale for each model run.

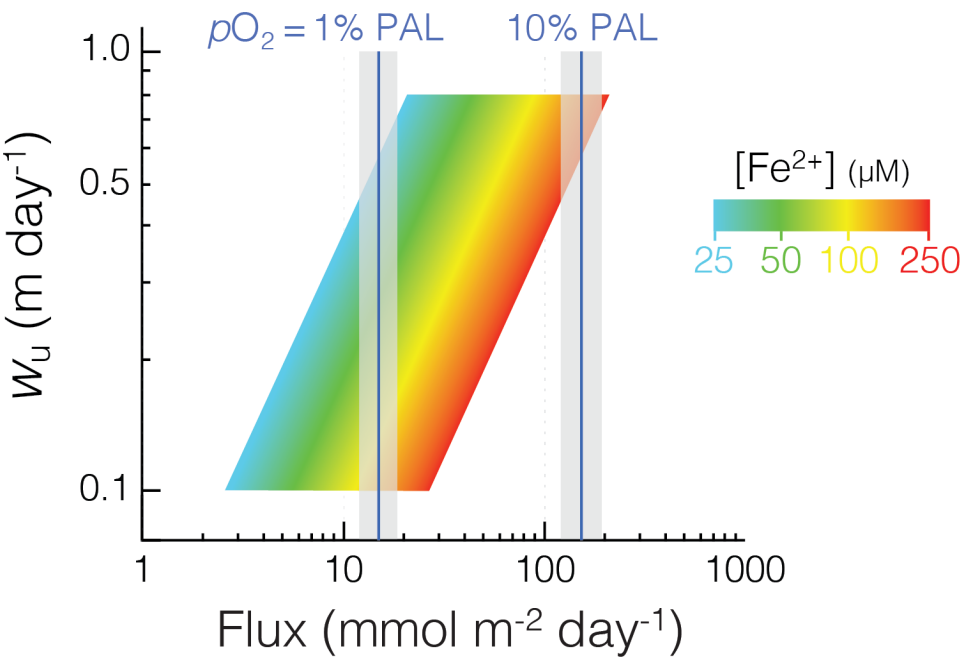

Fig. S2.

Comparison of the Fe flux calculated for upwelling Fe(II) as a function of upwelling velocity (w_u), and the downward flux of O_2 transferred across the air–sea interface as a function of pO_2. The Fe flux is shown for a range of long-term averaged upwelling velocities ($0.1 \leq w_u \leq 0.8$) considered reasonable for upwelling zones (*41*), and a wide range of values for deep marine [Fe^{2+}] levels (25–250 μM; shown in color gradient). The O_2 flux is shown at 25 ºC for pO_2 = 1 and pO_2 = 10 % PAL (blue lines) whereby the grey area represents the range relevant to seawater temperatures from 15–35 ºC. Assuming that 1 mole of O_2 (and secondary reactive oxygen species) can oxidize 4 moles of Fe^{2+}, these values show that for pO_2 = 1–10 % PAL the upwelling Fe(II) flux is only comparable to the downward flux of O_2 from the atmosphere at very high upwelling rates and [Fe^{2+}] levels.

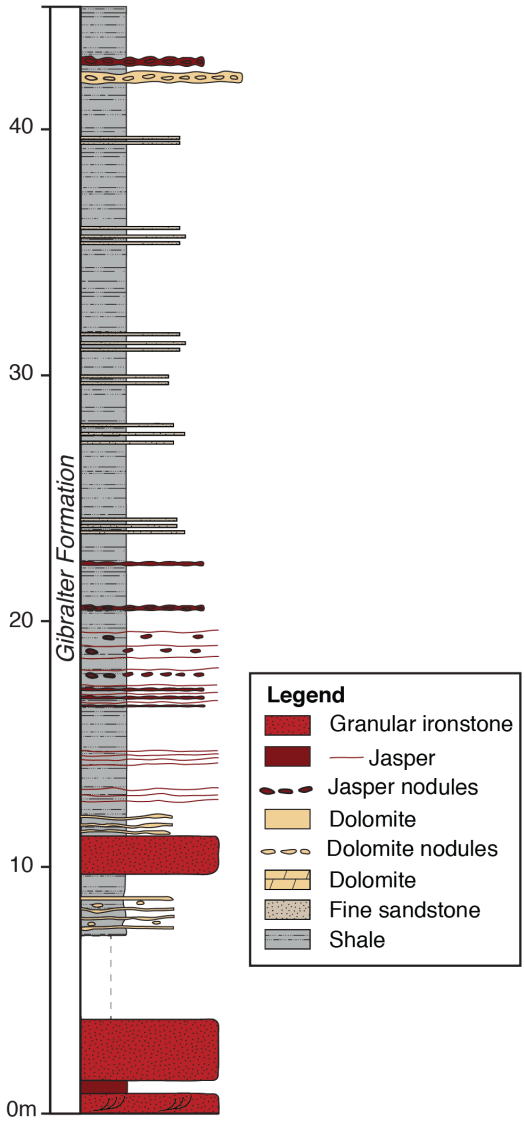

Fig. S3.
Stratigraphic section of the ironstone-bearing Gibralter Formation at East Arm (Great Slave Lake, Northwest Territories, Canada).

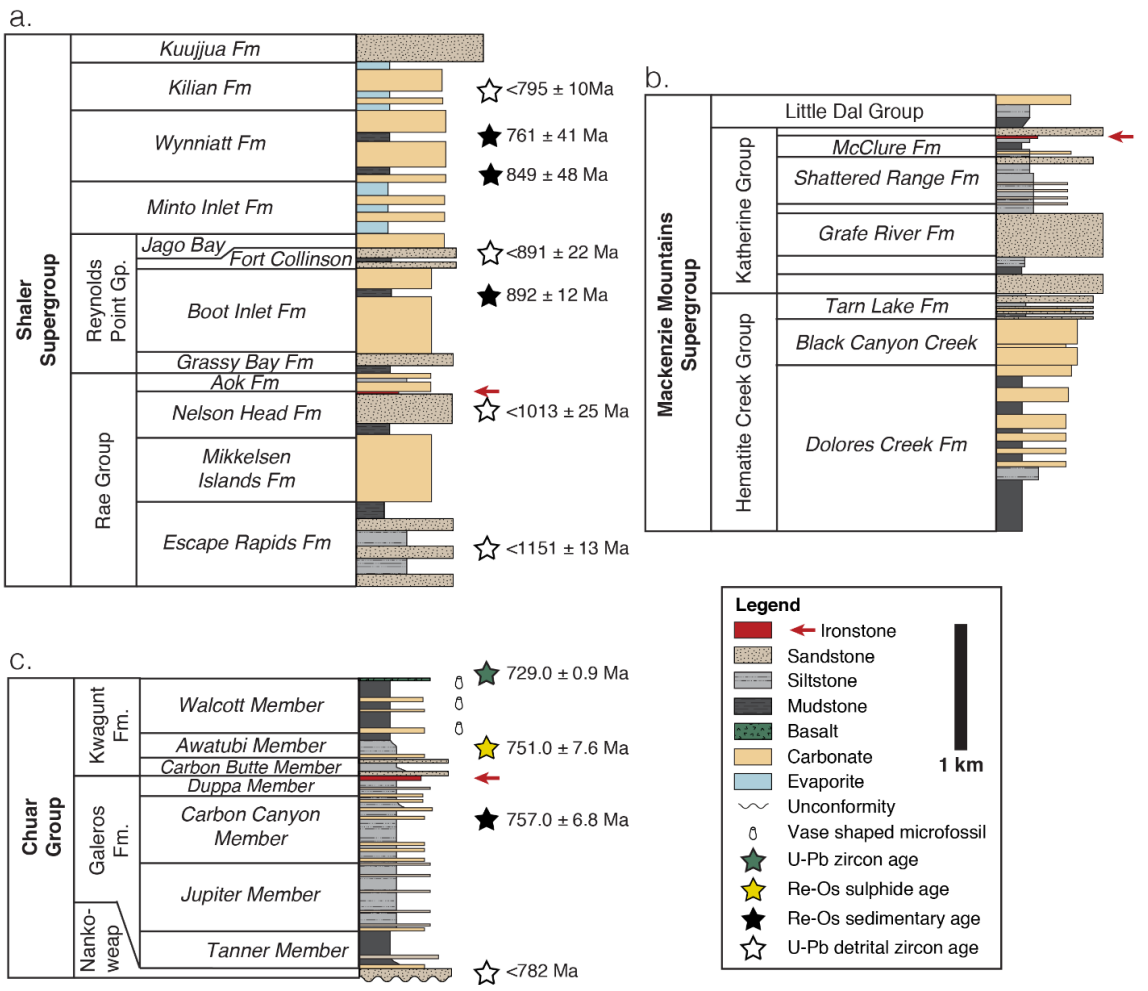

Fig. S4.

Schematic stratigraphic context of the studied Tonian ironstones within (a) the Nelson Head Formation in the Amundsen Basin (Northwest Territories and Nunavut, Canada); modified after Rainbird et al. (*104*) and Greenman et al. (*321*); (b) the McClure Formation in the Wernecke Mountains (Yukon, Canada); and (c) the Galeros Formation ironstone in the Grand Canyon (Arizona, USA); modified after Dehler et al. (*115*) and Rooney et al. (*124*).

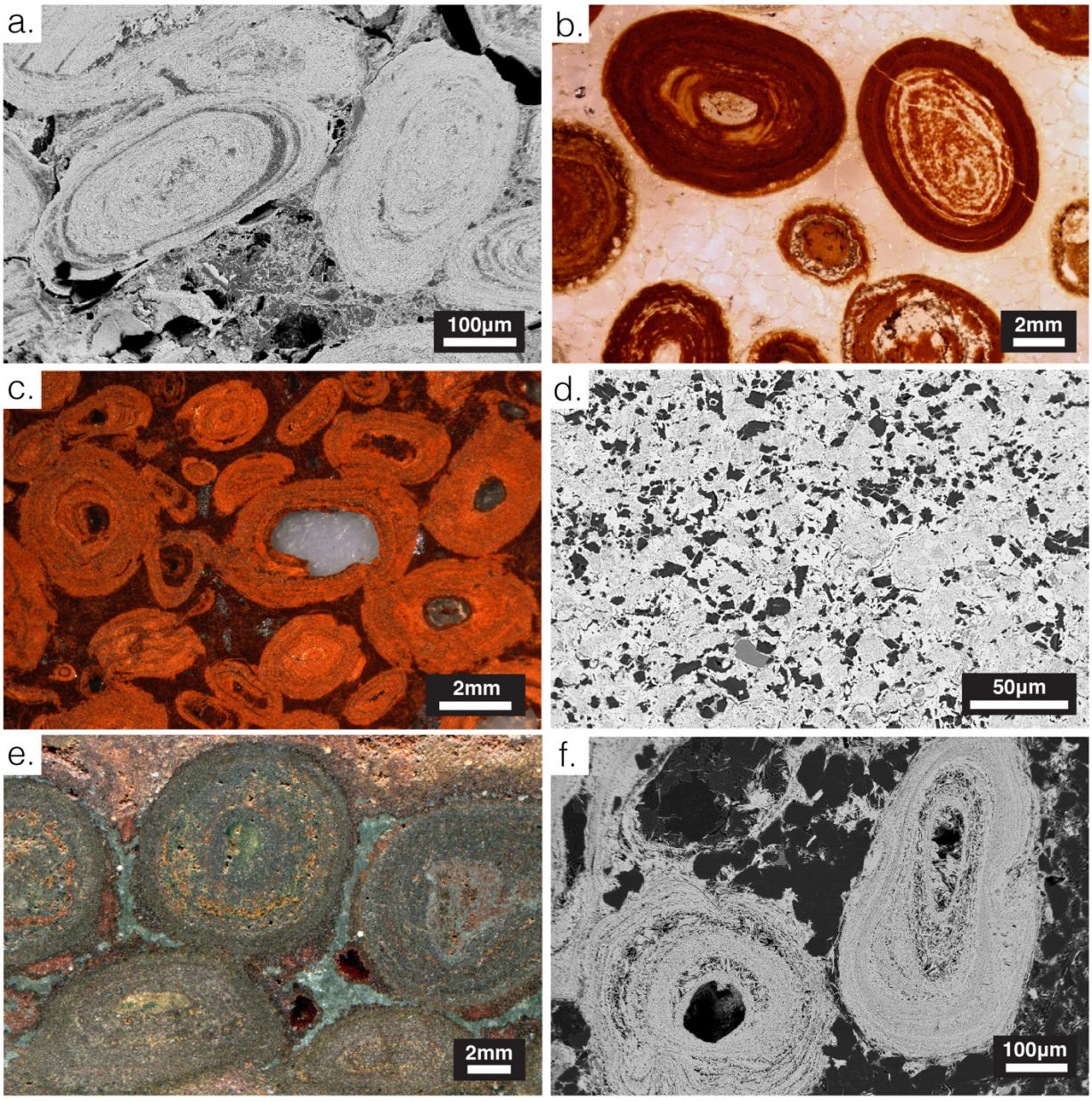

Fig. S5.

Sedimentology and petrography of the studied Proterozoic ironstones. (a) Backscattered electron (BSE) image showing concentric hematite laminae of Fe-ooids and uncoated detrital quartz grains in a clay-rich matrix in the ca. 1880 Ma Gibralter Formation. (b) Plain reflected light image of hematitic ooids in coarse-grained quartz matrix, ca. 1650 Ma Chuanlinggou Formation. (c) Plain reflected light image of hematitic ooids and pisoids set within a hematitic-silt matrix, ca. 1320 Ma Sherwin Formation. (d) BSE image of coarse hematite granules (grey) with a hematite cement (white) in a silica matrix (dark grey), upper ca. 900 Ma Nelson Head Formation. (e) Plain reflected light image of large, mixed Fe-pisoids within the ca. 900 McClure Formation, showing fine interlaminations of hematite with berthierine, with coarsely crystalline hematite cement. (f) BSE image of the ca. 750 Ma Galeros Formation Fe-ooids composed of hematite within a quartz sand matrix.

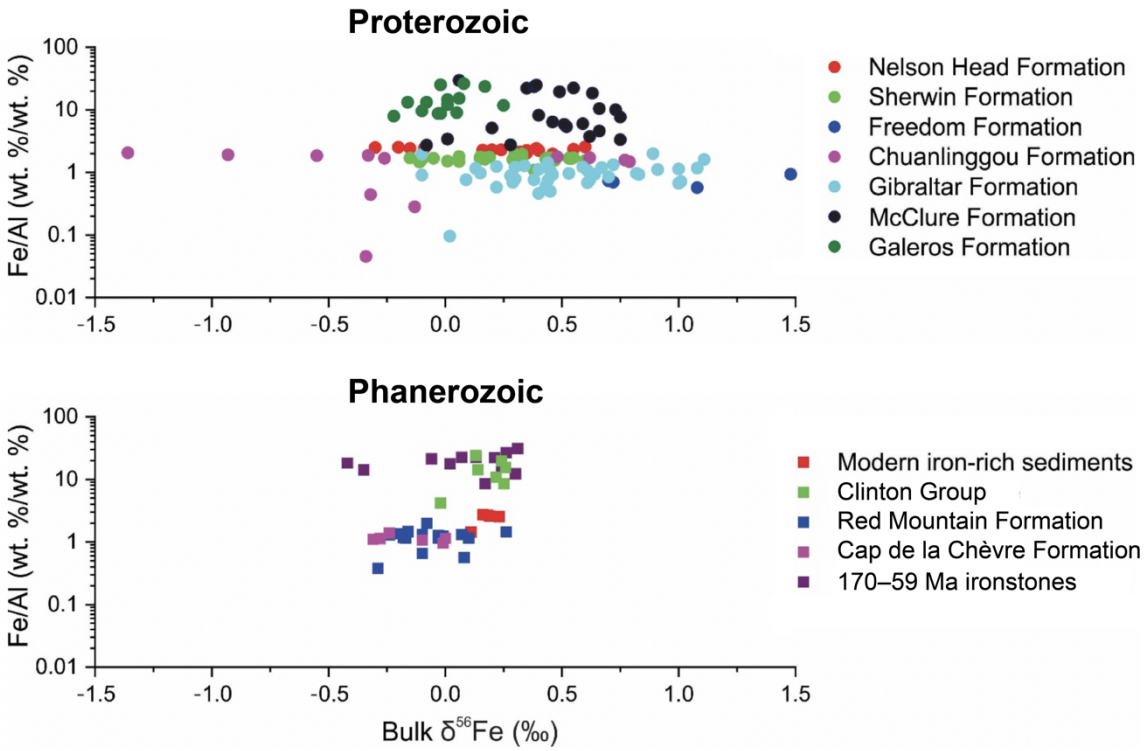

Fig. S6.

Cross-plot diagram of the relationship between Fe enrichment (Fe/Al) versus bulk rock Fe isotope composition (δ^{56}Fe values) of our studied Proterozoic and Phanerozoic ironstones and iron-rich sediments. The absence of a correlation between δ^{56}Fe values and Fe/Al ratios suggests no effect of a detrital input on the measured Fe isotope compositions.

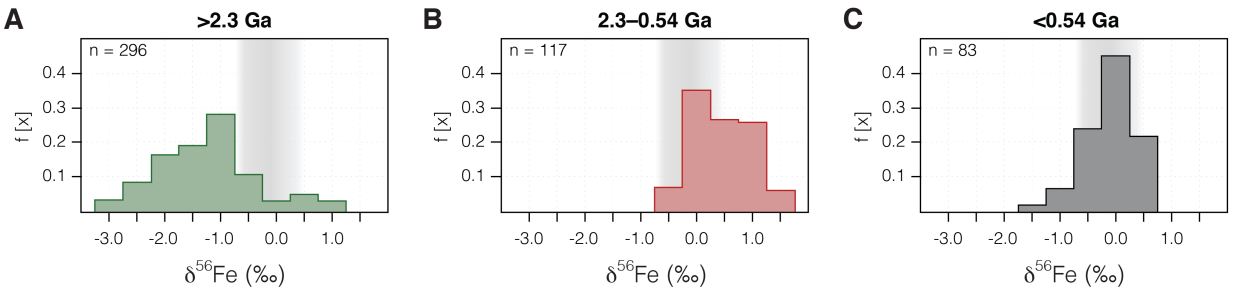

Fig. S7.

Relative frequency histograms showing the variation in δ^{56}Fe values of pyrite from marine sedimentary rocks (predominantly organic-rich shales) through time. (a) Pyrite from Archean–early Proterozoic (>2.2 Ga) marine sedimentary rocks, prior to and during the Great Oxidation Event. (b) Pyrite from marine sedimentary rocks deposited from the early to late Proterozoic (~2.2–0.54 Ga), after the Great Oxidation Event. (c) Pyrite from Phanerozoic (<0.54 Ga) marine sedimentary rocks. Note that pyrite Fe isotope data obtained by *in situ* analysis, which typically show a much greater variation in δ^{56}Fe values compared to bulk pyrite, are not included in this compilation. Pyrite Fe isotope data are updated from published compilations (*236, 277, 309*) with data from Zhang et al. (*322*) and Lin et al. (*323*).

Dataset S1. (separate file)

Bulk-rock Fe isotope data of the studied ironstones and iron-rich sediments.

Dataset S2. (separate file)

Selected major and trace element compositions of the studied ironstones and iron-rich sediments.

Dataset S3. (separate file)

Pyrite content of McClure Formation siliciclastic rocks.

Dataset S4. (separate file)

Results of statistical analyses of ironstone Fe isotope data.

SUPPLEMENTAL REFERENCES CITED

1. F. B. Van Houten, D. P. Bhattacharyya, Phanerozoic oolitic ironstones--geologic record and facies model. *Annual Review of Earth and Planetary Sciences* **10**, 441-457 (1982).
2. N. Galili *et al.*, The geologic history of seawater oxygen isotopes from marine iron oxides. *Science* **365**, 469-473 (2019).
3. D. B. Cole, B. O'Connell, N. J. Planavsky, Authigenic chromium enrichments in Proterozoic ironstones. *Sedimentary Geology* **372**, 25-43 (2018).
4. D. E. Canfield, R. Raiswell, J. T. Westrich, C. M. Reaves, R. A. Berner, The use of chromium reduction in the analysis of reduced inorganic sulfur in sediments and shales. *Chemical geology* **54**, 149-155 (1986).
5. D. Asael *et al.*, Coupled molybdenum, iron and uranium stable isotopes as oceanic paleoredox proxies during the Paleoproterozoic Shunga Event. *Chemical Geology* **362**, 193-210 (2013).
6. K. Dideriksen, J. Baker, S. Stipp, Iron isotopes in natural carbonate minerals determined by MC-ICP-MS with a 58Fe–54Fe double spike. *Geochimica et Cosmochimica Acta* **70**, 118-132 (2006).
7. M.-A. Millet, J. A. Baker, C. E. Payne, Ultra-precise stable Fe isotope measurements by high resolution multiple-collector inductively coupled plasma mass spectrometry with a 57Fe–58Fe double spike. *Chemical Geology* **304**, 18-25 (2012).
8. F. J. Millero, S. Sotolongo, M. Izaguirre, The oxidation kinetics of Fe (II) in seawater. *Geochimica et Cosmochimica Acta* **51**, 793-801 (1987).
9. E. J. Bellefroid *et al.*, Constraints on Paleoproterozoic atmospheric oxygen levels. *Proceedings of the National Academy of Sciences*, 201806216 (2018).
10. H. E. Garcia, L. I. Gordon, Oxygen solubility in seawater: Better fitting equations. *Limnology and oceanography* **37**, 1307-1312 (1992).
11. A. D. Czaja *et al.*, Evidence for free oxygen in the Neoarchean ocean based on coupled iron–molybdenum isotope fractionation. *Geochimica et Cosmochimica Acta* **86**, 118-137 (2012).
12. A. D. Czaja *et al.*, Biological Fe oxidation controlled deposition of banded iron formation in the ca. 3770 Ma Isua Supracrustal Belt (West Greenland). *Earth and Planetary Science Letters* **363**, 192-203 (2013).
13. A. D. Czaja, M. J. Van Kranendonk, B. L. Beard, C. M. Johnson, A multistage origin for Neoarchean layered hematite-magnetite iron formation from the Weld Range, Yilgarn Craton, Western Australia. *Chemical Geology* **488**, 125-137 (2018).
14. W. Li *et al.*, An anoxic, Fe (II)-rich, U-poor ocean 3.46 billion years ago. *Geochimica et Cosmochimica Acta* **120**, 65-79 (2013).
15. A. M. Satkoski, N. J. Beukes, W. Li, B. L. Beard, C. M. Johnson, A redox-stratified ocean 3.2 billion years ago. *Earth and Planetary Science Letters* **430**, 43-53 (2015).
16. A. W. Heard *et al.*, Triple iron isotope constraints on the role of ocean iron sinks in early atmospheric oxygenation. *Science* **370**, 446-449 (2020).
17. V. Busigny *et al.*, Origin of the Neoproterozoic Fulu Iron Formation, South China: Insights from Iron Isotopes and Rare Earth Element Patterns. *Geochimica et Cosmochimica Acta*, (2018).
18. B. Hales, L. Karp-Boss, A. Perlin, P. A. Wheeler, Oxygen production and carbon sequestration in an upwelling coastal margin. *Global Biogeochemical Cycles* **20**, (2006).
19. W. G. Whitman, The two-film theory of gas absorption. *Chem. Metall. Eng.* **29**, 146-148 (1923).
20. P. S. Liss, P. Slater, Flux of gases across the air-sea interface. *Nature* **247**, 181-184 (1974).
21. P. S. Liss, L. Merlivat, in *The role of air-sea exchange in geochemical cycling*. (Springer, 1986), pp. 113-127.

22. R. Wanninkhof, Relationship between wind speed and gas exchange over the ocean. *Journal of Geophysical Research: Oceans* **97**, 7373-7382 (1992).
23. R. Wanninkhof, Relationship between wind speed and gas exchange over the ocean revisited. *Limnology and Oceanography: Methods* **12**, 351-362 (2014).
24. R. Atlas *et al.*, A cross-calibrated, multiplatform ocean surface wind velocity product for meteorological and oceanographic applications. *Bulletin of the American Meteorological Society* **92**, 157-174 (2011).
25. T. Naegler, Reconciliation of excess 14C-constrained global CO2 piston velocity estimates. *Tellus B: Chemical and Physical Meteorology* **61**, 372-384 (2009).
26. C. Sweeney *et al.*, Constraining global air-sea gas exchange for CO2 with recent bomb 14C measurements. *Global Biogeochemical Cycles* **21**, (2007).
27. D. T. Ho *et al.*, Measurements of air-sea gas exchange at high wind speeds in the Southern Ocean: Implications for global parameterizations. *Geophysical Research Letters* **33**, (2006).
28. W. Hayduk, H. Laudie, Prediction of diffusion coefficients for nonelectrolytes in dilute aqueous solutions. *AIChE Journal* **20**, 611-615 (1974).
29. K. H. Coale, S. E. Fitzwater, R. M. Gordon, K. S. Johnson, R. T. Barber, Control of community growth and export production by upwelled iron in the equatorial Pacific Ocean. *Nature* **379**, 621-624 (1996).
30. R. M. Gordon, K. H. Coale, K. S. Johnson, Iron distributions in the equatorial Pacific: Implications for new production. *Limnology and Oceanography* **42**, 419-431 (1997).
31. F. Roquet, C. Wunsch, G. Madec, On the patterns of wind-power input to the ocean circulation. *Journal of physical oceanography* **41**, 2328-2342 (2011).
32. W. S. Broecker, T. Peng, Tracers in the a Sea. *Lamont-Doherty Geological Observatory*, (1982).
33. D. Kadko, Upwelling and primary production during the US GEOTRACES East Pacific Zonal Transect. *Global Biogeochemical Cycles* **31**, 218-232 (2017).
34. G. C. Johnson, M. J. McPhaden, E. Firing, Equatorial Pacific Ocean horizontal velocity, divergence, and upwelling. *Journal of Physical Oceanography* **31**, 839-849 (2001).
35. W. Z. Haskell II *et al.*, Upwelling velocity and eddy diffusivity from 7Be measurements used to compare vertical nutrient flux to export POC flux in the Eastern Tropical South Pacific. *Marine Chemistry* **168**, 140-150 (2015).
36. R. Steinfeldt, J. Sültenfuß, M. Dengler, T. Fischer, M. Rhein, Coastal upwelling off Peru and Mauritania inferred from helium isotope disequilibrium. *Biogeosciences* **12**, 7519-7533 (2015).
37. B. Klein, M. Rhein, Equatorial upwelling rates inferred from helium isotope data: A novel approach. *Geophysical research letters* **31**, (2004).
38. Z. Jing, Z. Hua, Y. Qi, X. Cheng, Numerical study on the coastal upwelling and its seasonal variation in the East China Sea. *Journal of Coastal Research*, 555-563 (2007).
39. W. Z. Haskell II, D. E. Hammond, M. G. Prokopenko, A dual-tracer approach to estimate upwelling velocity in coastal Southern California. *Earth and Planetary Science Letters* **422**, 138-149 (2015).
40. T. Tanhua, M. Liu, Upwelling velocity and ventilation in the Mauritanian upwelling system estimated by CFC-12 and SF6 observations. *Journal of Marine Systems* **151**, 57-70 (2015).
41. G. Froyland, R. M. Stuart, E. van Sebille, How well-connected is the surface of the global ocean? *Chaos: An Interdisciplinary Journal of Nonlinear Science* **24**, 033126 (2014).
42. D. Ianson, S. E. Allen, A two-dimensional nitrogen and carbon flux model in a coastal upwelling region. *Global Biogeochemical Cycles* **16**, 11-11-11-15 (2002).
43. D. E. Canfield, Models of oxic respiration, denitrification and sulfate reduction in zones of coastal upwelling. *Geochimica et Cosmochimica Acta* **70**, 5753-5765 (2006).
44. D. Z. Piper, P. K. Link, An upwelling model for the Phosphoria sea: A Permian, ocean-margin sea in the northwest United States. *AAPG bulletin* **86**, 1217-1235 (2002).
45. F. Chavez, Physical estimates of global new production: The upwelling contribution. *Upwelling in the ocean: modern processes and ancient records*, (1995).
46. J. Trabucho Alexandre *et al.*, The mid-Cretaceous North Atlantic nutrient trap: black shales and OAEs. *Paleoceanography* **25**, (2010).
47. H. D. Holland, *The chemical evolution of the atmosphere and oceans*. (Princeton University Press, 1984).
48. S. W. Poulton, P. W. Fralick, D. E. Canfield, Spatial variability in oceanic redox structure 1.8 billion years ago. *Nature Geoscience* **3**, 486 (2010).
49. H. Song *et al.*, The onset of widespread marine red beds and the evolution of ferruginous oceans. *Nature communications* **8**, 399 (2017).
50. N. J. Planavsky *et al.*, Widespread iron-rich conditions in the mid-Proterozoic ocean. *Nature* **477**, 448-451 (2011).
51. D. E. Canfield, The early history of atmospheric oxygen: homage to Robert M. Garrels. *Annu. Rev. Earth Planet. Sci.* **33**, 1-36 (2005).
52. L. A. Derry, Causes and consequences of mid-Proterozoic anoxia. *Geophysical Research Letters* **42**, 8538-8546 (2015).

53. B. Rasmussen, D. B. Meier, B. Krapež, J. R. Muhling, Iron silicate microgranules as precursor sediments to 2.5-billion-year-old banded iron formations. *Geology* **41**, 435-438 (2013).
54. N. J. Tosca, S. Guggenheim, P. K. Pufahl, An authigenic origin for Precambrian greenalite: Implications for iron formation and the chemistry of ancient seawater. *Bulletin* **128**, 511-530 (2016).
55. I. Halevy, M. Alesker, E. Schuster, R. Popovitz-Biro, Y. Feldman, A key role for green rust in the Precambrian oceans and the genesis of iron formations. *Nature Geoscience* **10**, 135-139 (2017).
56. A. Zegeye *et al.*, Green rust formation controls nutrient availability in a ferruginous water column. *Geology* **40**, 599-602 (2012).
57. C. Z. Jiang, N. J. Tosca, Fe (II)-carbonate precipitation kinetics and the chemistry of anoxic ferruginous seawater. *Earth and Planetary Science Letters* **506**, 231-242 (2019).
58. I. Halevy, A. Bachan, The geologic history of seawater pH. *Science* **355**, 1069-1071 (2017).
59. K. O. Konhauser *et al.*, Could bacteria have formed the Precambrian banded iron formations? *Geology* **30**, 1079-1082 (2002).
60. A. Kappler, C. Pasquero, K. O. Konhauser, D. K. Newman, Deposition of banded iron formations by anoxygenic phototrophic Fe (II)-oxidizing bacteria. *Geology* **33**, 865-868 (2005).
61. D. W. King, H. A. Lounsbury, F. J. Millero, Rates and mechanism of Fe (II) oxidation at nanomolar total iron concentrations. *Environmental science & technology* **29**, 818-824 (1995).
62. E. A. Sperling *et al.*, Statistical analysis of iron geochemical data suggests limited late Proterozoic oxygenation. *Nature* **523**, 451-454 (2015).
63. P. Hoffman, *Stratigraphy of the Lower Proterozoic (Aphebian), Great Slave Supergroup, East Arm of Great Slave Lake, District of Mackenzie*. (Department of Energy, Mines and Resources, 1968), vol. 68.
64. S. Roscoe, *Mineral resource assessment of the area in the East Arm (Great Slave Lake) and Artillery Lake region, NWT, proposed as a National Park (NTS 75 J, K, L, N, O)*. (Department of Energy, Mines and Resources, Geological Survey of Canada, 1987).
65. M. S. Dodd *et al.*, Organic remains in late Palaeoproterozoic granular iron formations and implications for the origin of granules. *Precambrian Research* **310**, 133-152 (2018).
66. O. van Breemen, B. Kjarsgaard, S. Tella, D. Lemkow, L. Aspler, U–Pb detrital zircon geochronology of clastic sedimentary rocks of the Paleoproterozoic Nonacho and East Arm basins, East Arm MERA study area, Chapter 4. *Mineral and energy resource assessment of the proposed Thaidene Nene National Park Reserve in the area of the east arm of Great Slave Lake, Northwest Territories. Geological Survey of Canada Open File* **7196**, 95-118 (2013).
67. S. Bowring, W. V. Schmus, P. Hoffman, U–Pb zircon ages from Athapuscow aulacogen, east arm of Great Slave Lake, NWT, Canada. *Canadian Journal of Earth Sciences* **21**, 1315-1324 (1984).
68. T. Clark, R. Wares, *Lithotectonic and metallogenic synthesis of the new Québec Orogen (Labrador Trough)*. (Géologie Québec [Ressources naturelles et faune Québec], 2006).
69. P. Pufahl, S. Anderson, E. Hiatt, Dynamic sedimentation of Paleoproterozoic continental margin iron formation, Labrador Trough, Canada: Paleoenvironments and sequence stratigraphy. *Sedimentary geology* **309**, 48-65 (2014).
70. A. Low, Report on exploration in the Labrador Peninsula a long Eastmain, Koksoak, Manikuagan and portions of other rivers. *Geological Survey of Canada, Annual Report, VI II, L* **98**, (1895).
71. U. Raye, P. K. Pufahl, T. K. Kyser, E. Ricard, E. E. Hiatt, The role of sedimentology, oceanography, and alteration on the δ56Fe value of the Sokoman Iron Formation, Labrador Trough, Canada. *Geochimica et Cosmochimica Acta* **164**, 205-220 (2015).
72. C. Klein, Greenalite, stilpnomelane, minnesotaite, crocidolite and carbonates in a very low-grade metamorphic Precambrian iron formation. *The Canadian Mineralogist* **12**, 475-498 (1974).
73. C. Klein, R. Fink, Petrology of the Sokoman Iron Formation in the Howells River area, at the western edge of the Labrador Trough. *Economic Geology* **71**, 453-487 (1976).
74. I. S. Zajac, The stratigraphy and mineralogy of the Sokoman Formation in the Knob Lake area, Quebec and Newfoundland. *Canada Geological Survey Bulletin* **220**, 151 (1974).
75. J. M. Findlay, R. R. Parrish, T. C. Birkett, D. H. Watanabe, U–Pb ages from the Nimish Formation and Montagnais glomeroporphyritic gabbro of the central New Québec Orogen, Canada. *Canadian Journal of Earth Sciences* **32**, 1208-1220 (1995).
76. D. Holm, D. Schneider, C. D. Coath, Age and deformation of Early Proterozoic quartzites in the southern Lake Superior region: Implications for extent of foreland deformation during final assembly of Laurentia. *Geology* **26**, 907-910 (1998).
77. N. J. Planavsky *et al.*, Low Mid-Proterozoic atmospheric oxygen levels and the delayed rise of animals. *science* **346**, 635-638 (2014).
78. J. Medaris, LG *et al.*, Late Paleoproterozoic climate, tectonics, and metamorphism in the southern Lake Superior region and Proto–North America: evidence from Baraboo interval quartzites. *The Journal of Geology* **111**, 243-257 (2003).
79. S. Zhang *et al.*, Pre-Rodinia supercontinent Nuna shaping up: a global synthesis with new paleomagnetic results from North China. *Earth and Planetary Science Letters* **353**, 145-155 (2012).

80. X. Chu, T. Zhang, Q. Zhang, T. W. Lyons, Sulfur and carbon isotope records from 1700 to 800 Ma carbonates of the Jixian section, northern China: Implications for secular isotope variations in Proterozoic seawater and relationships to global supercontinental events. *Geochimica et Cosmochimica Acta* **71**, 4668-4692 (2007).
81. Z. Li, X.-K. Zhu, Geochemical features of Xuanlong type iron ore deposit in Hebei Province and their geological significance. *Acta Petrologica Sinica* **28**, 2903-2911 (2012).
82. Y. Lin, D. Tang, X. Shi, X. Zhou, K. Huang, Shallow-marine ironstones formed by microaerophilic iron-oxidizing bacteria in terminal Paleoproterozoic. *Gondwana Research* **76**, 1-18 (2019).
83. C. Li *et al.*, Marine redox conditions in the middle Proterozoic ocean and isotopic constraints on authigenic carbonate formation: insights from the Chuanlinggou Formation, Yanshan Basin, North China. *Geochimica et Cosmochimica Acta* **150**, 90-105 (2015).
84. C. Duan *et al.*, U-Pb Ages and Hf Isotopes of Detrital Zircon Grains from the Mesoproterozoic Chuanlinggou Formation in North China Craton: Implications for the Geochronology of Sedimentary Iron Deposits and Crustal Evolution. *Minerals* **8**, 547 (2018).
85. L. Gao *et al.*, Recognition of Meso-and Neoproterozoic stratigraphic framework in North and South China. *Acta Geoscientica Sinica* **30**, 433-446 (2009).
86. Z. ShuanHong, Z. Yue, Y. Hao, H. JianMin, W. Fei, New constraints on ages of the Chuanlinggou and Tuanshanzi formations of the Changcheng System in the Yan-Liao area in the northern North China Craton. *Acta Petrologica Sinica* **29**, 2481-2490 (2013).
87. S. Abbott, I. Sweet, Tectonic control on third-order sequences in a siliciclastic ramp-style basin: An example from the Roper Superbasin (Mesoproterozoic), northern Australia. *Australian Journal of Earth Sciences* **47**, 637-657 (2000).
88. I. Sweet, T. Powell, Studies on petroleum geology and geochemistry, middle Proterozoic, McArthur Basin Northern Australia I: Petroleum potential. *The APPEA Journal* **28**, 283-302 (1988).
89. P. G. Betts, D. Giles, The 1800–1100 Ma tectonic evolution of Australia. *Precambrian Research* **144**, 92-125 (2006).
90. R. A. Spikings, D. A. Foster, B. P. Kohn, G. Lister, Post-orogenic (< 1500 Ma) thermal history of the Proterozoic Eastern fold belt, Mount Isa inlier, Australia. *Precambrian Research* **109**, 103-144 (2001).
91. R. Spikings, D. Foster, B. Kohn, G. Lister, Post-orogenic (< 1500 Ma) thermal history of the Palaeo-Mesoproterozoic, Mt. Isa province, NE Australia. *Tectonophysics* **349**, 327-365 (2002).
92. M. Jackson, M. MUIR, I. SWEET, in *12th International Sedimentological Congress*. (Bureau of Mineral Resources Canberra, 1986).
93. M. Ahmad, T. Munson, *Geology and mineral resources of the Northern Territory*. (Northern Territory Geological Survey, 2013).
94. F. Canavan, Iron ore deposits of Roper Bar. *Geology of Australian Ore Deposits* **1**, 212-215 (1965).
95. B. R. Johnson *et al.*, Phosphorus burial in ferruginous SiO2-rich Mesoproterozoic sediments. *Geology* **48**, 92-96 (2020).
96. G. M. Cox *et al.*, Basin redox and primary productivity within the Mesoproterozoic Roper Seaway. *Chemical Geology* **440**, 101-114 (2016).
97. A. J. Jarrett *et al.*, Microbial assemblage and palaeoenvironmental reconstruction of the 1.38 Ga Velkerri Formation, McArthur Basin, northern Australia. *Geobiology*, (2019).
98. K. Nguyen *et al.*, Absence of biomarker evidence for early eukaryotic life from the Mesoproterozoic Roper Group: Searching across a marine redox gradient in mid-Proterozoic habitability. *Geobiology* **17**, 247-260 (2019).
99. B. Yang *et al.*, Spatial and temporal variation in detrital zircon age provenance of the hydrocarbon-bearing upper Roper Group, Beetaloo Sub-basin, Northern Territory, Australia. *Precambrian Research* **304**, 140-155 (2018).
100. B. Kendall, R. A. Creaser, G. W. Gordon, A. D. Anbar, Re–Os and Mo isotope systematics of black shales from the Middle Proterozoic Velkerri and Wollogorang formations, McArthur Basin, northern Australia. *Geochimica et Cosmochimica Acta* **73**, 2534-2558 (2009).
101. R. H. Rainbird *et al.*, U–Pb geochronology of Riphean sandstone and gabbro from southeast Siberia and its bearing on the Laurentia–Siberia connection. *Earth and Planetary Science Letters* **164**, 409-420 (1998).
102. R. Rainbird, C. Jefferson, G. Young, The early Neoproterozoic sedimentary Succession B of northwestern Laurentia: Correlations and paleogeographic significance. *Geological Society of America Bulletin* **108**, 454-470 (1996).
103. J. Greenman, R. H. Rainbird, *Stratigraphy of the Upper Nelson Head, Aok, Grassy Bay, and Boot Inlet Formations in the Brock Inlier, Northwest Territories (NTS 97-A, D)*. (Geological Survey of Canada, 2018).
104. R. H. Rainbird, C. W. Jefferson, R. S. Hildebrand, J. K. Worth, The shaler supergroup and revision of Neoproterozoic stratigraphy in Amundsen Basin, Northwest Territories. *Current research, part C. Geological Survey of Canada, Paper*, 61-70 (1994).
105. C. Jefferson, G. Young, Late Proterozoic orange-weathering stromatolite biostrome Mackenzie Mountains and western Arctic Canada. (1988).

106. N. Rayner, R. Rainbird, U–Pb geochronology of the Shaler Supergroup, Victoria Island, northwest Canada: 2009–2013. *Geological Survey of Canada, Open File* **7419**, 10.4095 (2013).
107. D. van Acken, D. Thomson, R. H. Rainbird, R. A. Creaser, Constraining the depositional history of the Neoproterozoic Shaler Supergroup, Amundsen Basin, NW Canada: Rhenium-osmium dating of black shales from the Wynniatt and Boot Inlet Formations. *Precambrian Research* **236**, 124-131 (2013).
108. D. Long, E. Turner, Formal definition of the Neoproterozoic Mackenzie Mountains Supergroup (NWT), and formal stratigraphic nomenclature for terrigenous clastic units of the Katherine Group. *Geological Survey of Canada Open File 7113*, 40 (2012).
109. G. S. Hume, T. A. Link, *Canol geological investigations in the Mackenzie River area, Northwest Territories and Yukon*. (Canada Department of Mines and Resources, Mines and Geology Branch, 1945).
110. E. C. Turner, K. MacFarlane, L. Weston, C. Relf, Stratigraphy of the Mackenzie Mountains supergroup in the Wernecke Mountains, Yukon. *Yukon Exploration and Geology*, 207-231 (2010).
111. J. E. Milton, K. A. Hickey, S. A. Gleeson, R. M. Friedman, New U-Pb constraints on the age of the Little Dal Basalts and Gunbarrel-related volcanism in Rodinia. *Precambrian Research* **296**, 168-180 (2017).
112. G. P. Halverson, P. F. Hoffman, D. P. Schrag, A. C. Maloof, A. H. N. Rice, Toward a Neoproterozoic composite carbon-isotope record. *GSA Bulletin* **117**, 1181-1207 (2005).
113. F. A. Macdonald *et al.*, Calibrating the cryogenian. *Science* **327**, 1241-1243 (2010).
114. C. M. Dehler *et al.*, Neoproterozoic Chuar Group (~ 800–742 Ma), Grand Canyon: A record of cyclic marine deposition during global cooling and supercontinent rifting. *Sedimentary Geology* **141**, 465-499 (2001).
115. C. Dehler *et al.*, Synthesis of the 780–740 Ma Chuar, Uinta Mountain, and Pahrump (ChUMP) groups, western USA: implications for Laurentia-wide cratonic marine basins. *GSA Bulletin* **129**, 607-624 (2017).
116. T. D. Ford, W. J. Breed, Late Precambrian Chuar Group, Grand Canyon, Arizona. *Geological Society of America Bulletin* **84**, 1243-1260 (1973).
117. D. T. Johnston *et al.*, An emerging picture of Neoproterozoic ocean chemistry: Insights from the Chuar Group, Grand Canyon, USA. *Earth and Planetary Science Letters* **290**, 64-73 (2010).
118. S. M. Porter, A. H. Knoll, Testate amoebae in the Neoproterozoic Era: evidence from vase-shaped microfossils in the Chuar Group, Grand Canyon. *Paleobiology* **26**, 360-385 (2000).
119. S. M. Porter, L. A. Riedman, Systematics of organic-walled microfossils from the ca. 780–740 Ma Chuar Group, Grand Canyon, Arizona. *Journal of Paleontology* **90**, 815-853 (2016).
120. C. D. Walcott, *Pre-Cambrian Igneous Rocks of the Unkar Terrane, Grand Canyon of the Colorado, Arizona*. (US Government Printing Office, 1895).
121. N. Hinds, Researches on Algonkian formations of Grand Canyon National Park. *Carnegie Institution of Washington Yearbook* **32**, 325-328 (1933).
122. C. M. Dehler, S. M. Porter, J. M. Timmons, K. Karlstrom, The Neoproterozoic Earth system revealed from the Chuar Group of Grand Canyon. *Grand Canyon Geology: Two Billion Years of Earth's History: Geological Society of America Special Paper* **489**, 49-72 (2012).
123. D. T. Johnston *et al.*, An emerging picture of Neoproterozoic ocean chemistry: Insights from the Chuar Group, Grand Canyon, USA. *Earth and Planetary Science Letters* **290**, 64-73 (2010).
124. A. D. Rooney *et al.*, Coupled Re-Os and U-Pb geochronology of the Tonian Chuar Group, Grand Canyon. *GSA Bulletin* **130**, 1085-1098 (2018).
125. J. Cogné, N. Bonhommet, V. Kropacek, T. Zelinka, E. Petrovski, Paleomagnetism and magnetic fabric of the deformed redbeds of the Cap de la Chèvre formation, Brittany, France. *Physics of the earth and planetary interiors* **67**, 374-388 (1991).
126. A. Fernandez, J. J. Chauvel, M. C. Moro, Comparative study of the lower Ordovician ironstones of the Iberian massif (Zamora, Spain) and of the Armorican massif (Central Brittany, France). *Journal of sedimentary research* **68**, (1998).
127. J.-L. Bonjour, J.-J. Chauvel, Un exemple de sedimentation initiale dans un bassin paleozoique; etude petrographique et geochimique de l'Ordovicien inferieur de la presquile de Crozon (Finistere). *Bulletin de la Société géologique de France* **4**, 81-91 (1988).
128. J. Bonjour, J.-J. Peucat, J.-J. Chauvel, F. Paris, J. Cornichet, U-Pb zircon dating of the early paleozoic (Arenigian) transgression in Western Brittany (France): A new constraint for the lower paleozoic time-scale. *Chemical Geology: Isotope Geoscience section* **72**, 329-336 (1988).
129. T. M. Chowns, Sequence Stratigraphy of the Red Mountain Formation; Setting for the Origin of the Birmingham Ironstones. (2006).
130. T. M. Chowns, A. K. Rindsberg, Stratigraphy and depositional environments in the Silurian Red Mountain Formation of the southern Appalachian basin, USA. *Field Guides* **39**, 95-143 (2015).
131. B. G. Baarli, S. Brande, M. Johnson, Proximality trends in the Red Mountain Formation (Lower Silurian) of Birmingham, Alabama. *Oklahoma Geological Survey Bulletin* **145**, 1-17 (1992).
132. J. B. Maynard, Geochemistry of oolitic iron ores, an electron microprobe study. *Economic Geology* **81**, 1473-1483 (1986).
133. A. Mücke, F. Farshad, Whole-rock and mineralogical composition of Phanerozoic ooidal ironstones: comparison and differentiation of types and subtypes. *Ore Geology Reviews* **26**, 227-262 (2005).

134. T. M. Chowns, L. Hunt, J. Madden, A comparison by SEM of texture and composition in hematite and chamosite ooids from the Birmingham ironstones of Alabama, USA. *Geol. Soc. Am. Abstr. with Programs, Southeast. Sect. 60th Annu. Meet* **43**, 29 (2011).
135. C. E. Brett *et al.*, Early Silurian condensed intervals, ironstones, and sequence stratigraphy in the Appalachian foreland basin. *New York State Museum Bulletin* **491**, 89-143 (1998).
136. E. Cotter, J. E. Link, Deposition and diagenesis of Clinton ironstones (Silurian) in the Appalachian Foreland Basin of Pennsylvania. *Geological Society of America Bulletin* **105**, 911-922 (1993).
137. H. Muskatt, in *NY State Geol. Assoc. 44th Annu. Meet. Guidebook*. (1972), pp. A1-A37.
138. C. Brett, W. Goodman, T. Broadhead, S. Hageman, Silurian stratigraphy of the type Clinton area of central New York. *Sedimentary Environments of Silurian Taconia: University of Tennessee, Department of Geological Sciences, Studies in Geology* **26**, 200-230 (1996).
139. T. Gillette, *The Clinton of western and central New York*. (University of the State of New York, 1947).
140. L. V. Rickard, D. W. Fisher, Correlation of the Silurian and devonian rocks in New York State. (1975).
141. N. Sullivan, C. E. Brett, P. McLaughlin, in *Field Trip Guidebook for the 84th Annual Meeting of the New York State Geological Association, pp. B5–1–B5–40*. (2012).
142. C. H. Smythe, *On the genetic significance of ferrous silicate associated with the Clinton iron ores*. (University of the State of New York, 1919).
143. E. Cotter, Storm effects on siliciclastic and carbonate shelf sediments in the medial Silurian succession of Pennsylvania. *Sedimentary geology* **69**, 245-258 (1990).
144. P. I. McLaughlin, P. Emsbo, C. E. Brett, Beyond black shales: the sedimentary and stable isotope records of oceanic anoxic events in a dominantly oxic basin (Silurian; Appalachian Basin, USA). *Palaeogeography, Palaeoclimatology, Palaeoecology* **367**, 153-177 (2012).
145. R. Schoen, Harvard University, (1962).
146. J. Maynard, Geochemistry of sedimentary ore deposits. (1983).
147. B. Reichenbach, Die Fossilien des Kahlenbergs–Teil A: Die Kopffüßer. *Der Kahlenberg und seine Schätze, Ringsheim, Zweckverband Abfallbeseitigung Kahlenberg*, 77-166 (1998).
148. V. Dietze, M. Kutz, M. Franz, K. Bosch, Stratigraphy of the Kahlenberg near Ringsheim (Upper Rhine Valley, SW Germany) with emphasis on the Laeviuscula and Sauzei zones (Lower Bajocian, Middle Jurassic). *Palaeodiversity* **2**, 19-65 (2009).
149. K. Sauer, Verlag nicht ermittelbar, (1948).
150. A. Bonte, J. Hatrival, Notice explicative de la feuille Rethel à 1/50000. *Carte géologique de la France BRG M. Orléans* **29**, 1-12 (1966).
151. U. Bayer, Stratigraphic and environmental patterns of ironstone deposits. *Geological Society, London, Special Publications* **46**, 105-117 (1989).
152. P. Courville, A. Bonnot, J.-C. Dudicourt, G. Cuif, in *Annales de Paléontologie*. (Elsevier, 2011), vol. 97, pp. 9-33.
153. J. K. Hall, V. A. Krasheninnikov, F. Hirsch, C. Benjamini, A. Flexer, Geological framework of the Levant, volume II: the Levantine Basin and Israel. *Historical Productions, Jerusalem*, (2005).
154. A. Sneh, R. Weinberger, Geology of the Metulla quadrangle, northern Israel: Implications for the offset along the Dead Sea Rift. *Israel Journal of Earth Sciences* **52**, (2003).
155. M. Bachmann, F. Hirsch, Lower Cretaceous carbonate platform of the eastern Levant (Galilee and the Golan Heights): stratigraphy and second-order sea-level change. *Cretaceous Research* **27**, 487-512 (2006).
156. A. Rosenfeld, F. Hirsch, The cretaceous of Israel. *Geological Framework of the Levant* **2**, 393-436 (2005).
157. V. Krassilov, E. Schrank, New Albian macro-and palynoflora from the Negev (Israel) with description of a new gymnosperm morphotaxon. *Cretaceous Research* **32**, 13-29 (2011).
158. G. Weinberger, A. Flexer, A. Livnat, The value of bivariate methods for identification and discrimination of fluvial sandstones from the Lower Cretaceous Hatira Formation, northern Negev. *Israel. Newsl. Stratigr.* **21**, 175-185 (1990).
159. B. Kafle, R. Olson, O. Catuneanu, G. Plint, Stratigraphy of the Bad Heart Formation, Clear Hills and Smoky River areas, Alberta. *Bulletin of Canadian Petroleum Geology* **61**, 253-282 (2013).
160. W. S. Donaldson, A. G. Plint, F. J. Longstaffe, Basement tectonic control on distribution of the shallow marine Bad Heart Formation: Peace River Arch area, northwest Alberta. *Bulletin of Canadian Petroleum Geology* **46**, 576-598 (1998).
161. J. Sliwinski, C. Gunning, K. Sheridan, B. Caplan, B. Smith, in *Geo Canada Abstract Joint Convention*. (2010).
162. W. Cobban, T. Dyman, K. Porter, Paleontology and stratigraphy of upper Coniacian–middle Santonian ammonite zones and application to erosion surfaces and marine transgressive strata in Montana and Alberta. *Cretaceous Research* **26**, 429-449 (2005).
163. W. Cobban, Diversity and distribution of Late Cretaceous ammonites, Western Interior, United States. *Geological Association of Canada, Special Paper* **39**, 435-451 (1993).
164. N. Belous *et al.*, The Western-Siberian iron ore basin. *Siberian Branch of the Academy of Sciences of the USSR, Novosibirsk ((448 pp.)(in Russia))*, (1964).

165. M. Rudmin, A. Mazurov, S. Banerjee, Origin of ooidal ironstones in relation to warming events: Cretaceous-Eocene Bakchar deposit, south-east Western Siberia. *Marine and Petroleum Geology* **100**, 309-325 (2019).
166. Z. Gnibidenko, N. Lebedeva, A. Levicheva, Magnetostratigraphy of the Campanian–Maastrichtian Bakchar Basin (southeastern West Siberia). *Russian Geology and Geophysics* **56**, 1652-1661 (2015).
167. N. Lebedeva, O. Kuzmina, E. Sobolev, I. Khazina, Stratigraphy of Upper Cretaceous and Cenozoic deposits of the Bakchar iron ore deposit (southwestern Siberia): New data. *Stratigraphy and Geological Correlation* **25**, 76-98 (2017).
168. R. Sheldon, Sedimentation of iron-rich rocks of Llandovery age (Lower Silurian) in the southern Appalachian basin. *Correlation of the Northern American Silurian Rocks: Geological Society of America Special Paper* **102**, 107-112 (1970).
169. A. Hallam, M. Bradshaw, Bituminous shales and oolitic ironstones as indicators of transgressions and regressions. *Journal of the Geological Society* **136**, 157-164 (1979).
170. T. Young, Eustatically controlled ooidal ironstone deposition: facies relationships of the Ordovician open-shelf ironstones of Western Europe. *Geological Society, London, Special Publications* **46**, 51-63 (1989).
171. K. G. Taylor, C. D. Curtis, Stability and facies association of early diagenetic mineral assemblages; an example from a Jurassic ironstone-mudstone succession, UK. *Journal of Sedimentary Research* **65**, 358-368 (1995).
172. J. Macquaker, K. Taylor, T. Young, C. Curtis, Sedimentological and geochemical controls on ooidal ironstone and 'bone-bed'formation and some comments on their sequence-stratigraphical significance. *Geological Society, London, Special Publications* **103**, 97-107 (1996).
173. W. S. Donaldson, A. G. Plint, F. J. Longstaffe, Tectonic and eustatic control on deposition and preservation of Upper Cretaceous ooidal ironstone and associated facies: Peace River Arch area, NW Alberta, Canada. *Sedimentology* **46**, 1159-1182 (1999).
174. P. Collin, J. Loreau, P. Courville, Depositional environments and iron ooid formation in condensed sections (Callovian–Oxfordian, south-eastern Paris basin, France). *Sedimentology* **52**, 969-985 (2005).
175. P. K. Pufahl, F. Pirajno, E. E. Hiatt, Riverine mixing and fluvial iron formation: A new type of Precambrian biochemical sediment. *Geology* **41**, 1235-1238 (2013).
176. S. J. Akin, P. K. Pufahl, E. E. Hiatt, F. Pirajno, Oxygenation of shallow marine environments and chemical sedimentation in Palaeoproterozoic peritidal settings: Frere Formation, Western Australia. *Sedimentology* **60**, 1559-1582 (2013).
177. W. Salama, M. El Aref, R. Gaupp, Facies analysis and palaeoclimatic significance of ironstones formed during the Eocene greenhouse. *Sedimentology* **61**, 1594-1624 (2014).
178. A. H. Rahiminejad, H. Zand-Moghadam, Synsedimentary formation of ooidal ironstone: an example from the Jurassic deposits of SE central Iran. *Ore Geology Reviews* **95**, 238-257 (2018).
179. S. Todd, P. Pufahl, J. Murphy, K. Taylor, Sedimentology and oceanography of early Ordovician ironstone, Bell Island, Newfoundland: Ferruginous seawater and upwelling in the Rheic Ocean. *Sedimentary Geology* **379**, 1-15 (2019).
180. B. W. Sellwood, Regional environmental changes across a Lower Jurassic stage-boundary in Britain. *Palaeontology* **15**, 125 (1972).
181. A. Smith *et al.*, Oncoidal granular iron formation in the Mesoarchaean Pongola Supergroup, southern Africa: Textural and geochemical evidence for biological activity during iron deposition. *Geobiology* **15**, 731-749 (2017).
182. A. Kearsley, Iron-rich ooids, their mineralogy and microfabric: clues to their origin and evolution. *Geological Society, London, Special Publications* **46**, 141-164 (1989).
183. J. M. Heikoop, C. J. Tsujita, M. J. Risk, T. Tomascik, A. J. Mah, Modern iron ooids from a shallow-marine volcanic setting: Mahengetang, Indonesia. *Geology* **24**, 759-762 (1996).
184. U. Sturesson, A. Dronov, T. Saadre, Lower Ordovician iron ooids and associated oolitic clays in Russia and Estonia: a clue to the origin of iron oolites? *Sedimentary Geology* **123**, 63-80 (1999).
185. E. Kalińska-Nartiša, N. Stivrins, I. Grudzinska, Quartz grains reveal sedimentary palaeoenvironment and past storm events: A case study from eastern Baltic. *Estuarine, Coastal and Shelf Science* **200**, 359-370 (2018).
186. A. Garcia-Frank, S. Ureta, R. Mas, Iron-coated particles from condensed Aalenian–Bajocian deposits: evolutionary model (Iberian Basin, Spain). *Journal of Sedimentary Research* **82**, 953-968 (2012).
187. K. Dahanayake, W. E. Krumbein, Microbial structures in oolitic iron formations. *Mineralium Deposita* **21**, 85-94 (1986).
188. R. M. Burkhalter, Ooidal ironstones and ferruginous microbialites: origin and relation to sequence stratigraphy (Aalenian and Bajocian, Swiss Jura mountains). *Sedimentology* **42**, 57-74 (1995).
189. D. Spears, Aspects of iron incorporation into sediments with special reference to the Yorkshire Ironstones. *Geological Society, London, Special Publications* **46**, 19-30 (1989).
190. C. Hughes, The application of analytical transmission electron microscopy to the study of oolitic ironstones: a preliminary study. *Geological Society, London, Special Publications* **46**, 121-131 (1989).

191. E. Garzanti, Himalayan ironstones," superplumes," and the breakup of Gondwana. *Geology* **21**, 105-108 (1993).
192. M. Reolid, I. Abad, J. M. Martín-García, Palaeoenvironmental implications of ferruginous deposits related to a Middle–Upper Jurassic discontinuity (Prebetic Zone, Betic Cordillera, southern Spain). *Sedimentary Geology* **203**, 1-16 (2008).
193. B. M. Simonson, A. Goode, First discovery of ferruginous chert arenites in the early Precambrian Hamersley Group of Western Australia. *Geology* **17**, 269-272 (1989).
194. S. C. Meyer, D. A. Textoris, J. M. Dennison, Lithofacies of the Silurian Keefer Sandstone, east-central Appalachian basin, USA. *Sedimentary geology* **76**, 187-206 (1992).
195. P. K. Pufahl, P. W. Fralick, Depositional controls on Palaeoproterozoic iron formation accumulation, Gogebic Range, Lake Superior region, USA. *Sedimentology* **51**, 791-808 (2004).
196. M. Rudmin *et al.*, Ooidal ironstones in the Meso-Cenozoic sequences in western Siberia: assessment of formation processes and relationship with regional and global earth processes. *Journal of Palaeogeography* **9**, 1-21 (2020).
197. J. Catt, M. Gad, H. Le Riche, A. Lord, Geochemistry, micropalaeontology and origin of the middle Lias ironstones in northeast Yorkshire (Great Britain). *Chemical Geology* **8**, 61-76 (1971).
198. A. Mücke, Chamosite, siderite and the environmental conditions of their formation in chamosite-type Phanerozoic ooidal ironstones. *Ore Geology Reviews* **28**, 235-249 (2006).
199. K. Konhauser *et al.*, Iron formations: A global record of Neoarchaean to Palaeoproterozoic environmental history. *Earth-Science Reviews* **172**, 140-177 (2017).
200. E. Cotter, Diagenetic alteration of chamositic clay minerals to ferric oxide in oolitic ironstone. *Journal of Sedimentary Research* **62**, 54-60 (1992).
201. H. E. James Jr, F. B. Van Houten, Miocene goethitic and chamositic oolites, northeastern Colombia. *Sedimentology* **26**, 125-133 (1979).
202. U. Sturesson, J. Heikoop, M. Risk, Modern and Palaeozoic iron ooids—a similar volcanic origin. *Sedimentary Geology* **136**, 137-146 (2000).
203. A. Siehl, J. Thein, Minette-type ironstones. *Geological Society, London, Special Publications* **46**, 175-193 (1989).
204. M. Boso, C. Monaldi, in *Stratabound ore deposits in the Andes*. (Springer, 1990), pp. 175-186.
205. P. K. Pufahl *et al.*, Ordovician ironstone of the Iberian margin: Coastal upwelling, ocean anoxia and Palaeozoic biodiversity. *The Depositional Record* **6**, 581-604 (2020).
206. H. Harder, Mineral genesis in ironstones: a model based upon laboratory experiments and petrographic observations. *Geological Society, London, Special Publications* **46**, 9-18 (1989).
207. D. P. Bhattacharyya, Origin of berthierine in ironstones. *Clays and clay minerals* **31**, 173-182 (1983).
208. C. Johnson, B. Beard, S. Weyer, in *Iron Geochemistry: An Isotopic Perspective*. (Springer, 2020), pp. 1-360.
209. S. W. Poulton, D. E. Canfield, Ferruginous conditions: a dominant feature of the ocean through Earth's history. *Elements* **7**, 107-112 (2011).
210. E. A. Sperling *et al.*, Statistical analysis of iron geochemical data suggests limited late Proterozoic oxygenation. *Nature* **523**, 451 (2015).
211. T. W. Lyons, C. T. Reinhard, N. J. Planavsky, The rise of oxygen in Earth's early ocean and atmosphere. *Nature* **506**, 307 (2014).
212. W. B. Berry, P. Wilde, Progressive ventilation of the oceans; an explanation for the distribution of the lower Paleozoic black shales. *American Journal of Science* **278**, 257-275 (1978).
213. L. R. Kump, W. E. Seyfried, Hydrothermal Fe fluxes during the Precambrian: effect of low oceanic sulfate concentrations and low hydrostatic pressure on the composition of black smokers. *Earth and Planetary Science Letters* **235**, 654-662 (2005).
214. S. W. Poulton *et al.*, A continental-weathering control on orbitally driven redox-nutrient cycling during Cretaceous Oceanic Anoxic Event 2. *Geology* **43**, 963-966 (2015).
215. M. Clarkson *et al.*, Dynamic anoxic ferruginous conditions during the end-Permian mass extinction and recovery. *Nature Communications* **7**, 1-9 (2016).
216. F. Van Houten, M. A. Arthur, Temporal patterns among Phanerozoic oolitic ironstones and oceanic anoxia. *Geological Society, London, Special Publications* **46**, 33-49 (1989).
217. M. B. Abram, M. Holz, Early to Middle Devonian ironstone and phosphorite in the northwestern Gondwana Parnaíba Basin, Brazil: A record of an epeiric margin paleoceanographic changes. *Sedimentary Geology* **402**, 105646 (2020).
218. H. Borchert, Formation of marine sedimentary iron ores. *Chemical oceanography* **2**, 159-204 (1965).
219. E. Matheson, P. K. Pufahl, Clinton ironstone revisited and implications for Silurian Earth system evolution. *Earth Science Reviews*, (2021).
220. T. Williams, R. Owen, Authigenesis of ferric oolites in superficial sediments from Lake Malawi, Central Africa. *Chemical geology* **89**, 179-188 (1990).
221. T. P. Young, Phanerozoic ironstones: an introduction and review. *Geological Society, London, Special Publications* **46**, ix-xxv (1989).

222. S. W. Poulton, R. Raiswell, Chemical and physical characteristics of iron oxides in riverine and glacial meltwater sediments. *Chemical Geology* **218**, 203-221 (2005).
223. R. Raiswell, Iron transport from the continents to the open ocean: The aging–rejuvenation cycle. *Elements* **7**, 101-106 (2011).
224. E. Boyle, J. Edmond, E. Sholkovitz, The mechanism of iron removal in estuaries. *Geochimica et Cosmochimica Acta* **41**, 1313-1324 (1977).
225. H. C. Dorland, University of Johannesburg, (1999).
226. V. A. Elrod, W. M. Berelson, K. H. Coale, K. S. Johnson, The flux of iron from continental shelf sediments: A missing source for global budgets. *Geophysical Research Letters* **31**, (2004).
227. S. Severmann, J. McManus, W. M. Berelson, D. E. Hammond, The continental shelf benthic iron flux and its isotope composition. *Geochimica et Cosmochimica Acta* **74**, 3984-4004 (2010).
228. A. Noffke *et al.*, Benthic iron and phosphorus fluxes across the Peruvian oxygen minimum zone. *Limnology and Oceanography* **57**, 851-867 (2012).
229. P. J. Lam, J. K. Bishop, The continental margin is a key source of iron to the HNLC North Pacific Ocean. *Geophysical Research Letters* **35**, (2008).
230. S. Siedlecki, A. Mahadevan, D. Archer, Mechanism for export of sediment-derived iron in an upwelling regime. *Geophysical research letters* **39**, (2012).
231. W. B. Homoky, S. G. John, T. M. Conway, R. A. Mills, Distinct iron isotopic signatures and supply from marine sediment dissolution. *Nature communications* **4**, 1-10 (2013).
232. T. M. Conway, S. G. John, Quantification of dissolved iron sources to the North Atlantic Ocean. *Nature* **511**, 212-215 (2014).
233. C. M. Johnson, B. L. Beard, E. E. Roden, The iron isotope fingerprints of redox and biogeochemical cycling in modern and ancient Earth. *Annu. Rev. Earth Planet. Sci.* **36**, 457-493 (2008).
234. S. M. McLennan, Relationships between the trace element composition of sedimentary rocks and upper continental crust. *Geochemistry, Geophysics, Geosystems* **2**, (2001).
235. L. Wu, B. L. Beard, E. E. Roden, C. M. Johnson, Stable iron isotope fractionation between aqueous Fe (II) and hydrous ferric oxide. *Environmental science & technology* **45**, 1847-1852 (2011).
236. N. Dauphas, S. G. John, O. Rouxel, Iron isotope systematics. *Reviews in Mineralogy and Geochemistry* **82**, 415-510 (2017).
237. N. Dauphas, O. Rouxel, Mass spectrometry and natural variations of iron isotopes. *Mass Spectrometry Reviews* **25**, 515-550 (2006).
238. A. J. Frierdich, B. L. Beard, T. R. Reddy, M. M. Scherer, C. M. Johnson, Iron isotope fractionation between aqueous Fe (II) and goethite revisited: New insights based on a multi-direction approach to equilibrium and isotopic exchange rate modification. *Geochimica et Cosmochimica Acta* **139**, 383-398 (2014).
239. B. L. Beard, C. M. Johnson, K. L. Von Damm, R. L. Poulson, Iron isotope constraints on Fe cycling and mass balance in oxygenated Earth oceans. *Geology* **31**, 629-632 (2003).
240. S. Severmann *et al.*, The effect of plume processes on the Fe isotope composition of hydrothermally derived Fe in the deep ocean as inferred from the Rainbow vent site, Mid-Atlantic Ridge, 36 14′ N. *Earth and Planetary Science Letters* **225**, 63-76 (2004).
241. B. L. Beard, C. M. Johnson, Fe isotope variations in the modern and ancient earth and other planetary bodies. *Reviews in Mineralogy and Geochemistry* **55**, 319-357 (2004).
242. O. Rouxel, W. C. Shanks III, W. Bach, K. J. Edwards, Integrated Fe-and S-isotope study of seafloor hydrothermal vents at East Pacific Rise 9–10 N. *Chemical Geology* **252**, 214-227 (2008).
243. Y. Gong, Y. Xia, F. Huang, H. Yu, Average iron isotopic compositions of the upper continental crust: constrained by loess from the Chinese Loess Plateau. *Acta Geochimica* **36**, 125-131 (2017).
244. B. L. Beard *et al.*, Iron isotope biosignatures. *Science* **285**, 1889-1892 (1999).
245. G. Icopini, A. Anbar, S. Ruebush, M. Tien, S. L. Brantley, Iron isotope fractionation during microbial reduction of iron: the importance of adsorption. *Geology* **32**, 205-208 (2004).
246. H. A. Crosby, E. E. Roden, C. M. Johnson, B. L. Beard, The mechanisms of iron isotope fractionation produced during dissimilatory Fe (III) reduction by Shewanella putrefaciens and Geobacter sulfurreducens. *Geobiology* **5**, 169-189 (2007).
247. H. A. Crosby, C. M. Johnson, E. E. Roden, B. L. Beard, Coupled Fe (II)− Fe (III) electron and atom exchange as a mechanism for Fe isotope fractionation during dissimilatory iron oxide reduction. *Environmental science & technology* **39**, 6698-6704 (2005).
248. B. N. Revels, D. C. Ohnemus, P. J. Lam, T. M. Conway, S. G. John, The isotopic signature and distribution of particulate iron in the North Atlantic Ocean. *Deep Sea Research Part II: Topical Studies in Oceanography* **116**, 321-331 (2015).
249. E. L. Rue, K. W. Bruland, Complexation of iron (III) by natural organic ligands in the Central North Pacific as determined by a new competitive ligand equilibration/adsorptive cathodic stripping voltammetric method. *Marine chemistry* **50**, 117-138 (1995).
250. M. Labatut *et al.*, Iron sources and dissolved-particulate interactions in the seawater of the Western Equatorial Pacific, iron isotope perspectives. *Global Biogeochemical Cycles* **28**, 1044-1065 (2014).

251. K. Dideriksen, J. A. Baker, S. L. S. Stipp, Equilibrium Fe isotope fractionation between inorganic aqueous Fe (III) and the siderophore complex, Fe (III)-desferrioxamine B. *Earth and Planetary Science Letters* **269**, 280-290 (2008).
252. J. L. Morgan, L. E. Wasylenki, J. Nuester, A. D. Anbar, Fe isotope fractionation during equilibration of Fe−organic complexes. *Environmental science & technology* **44**, 6095-6101 (2010).
253. S. M. Ilina *et al.*, Extreme iron isotope fractionation between colloids and particles of boreal and temperate organic-rich waters. *Geochimica et Cosmochimica Acta* **101**, 96-111 (2013).
254. R. Escoube *et al.*, Iron isotope systematics in Arctic rivers. *Comptes Rendus Geoscience* **347**, 377-385 (2015).
255. B. Bergquist, E. Boyle, Iron isotopes in the Amazon River system: weathering and transport signatures. *Earth and Planetary Science Letters* **248**, 54-68 (2006).
256. C. Hirst *et al.*, Characterisation of Fe-bearing particles and colloids in the Lena River basin, NE Russia. *Geochimica et Cosmochimica Acta* **213**, 553-573 (2017).
257. A. Radic, F. Lacan, J. W. Murray, Iron isotopes in the seawater of the equatorial Pacific Ocean: New constraints for the oceanic iron cycle. *Earth and Planetary Science Letters* **306**, 1-10 (2011).
258. J. A. Hawkes, D. Connelly, M. Gledhill, E. P. Achterberg, The stabilisation and transportation of dissolved iron from high temperature hydrothermal vent systems. *Earth and Planetary Science Letters* **375**, 280-290 (2013).
259. S. G. Sander, A. Koschinsky, Metal flux from hydrothermal vents increased by organic complexation. *Nature Geoscience* **4**, 145-150 (2011).
260. M. Staubwasser, R. Schoenberg, F. von Blanckenburg, S. Krüger, C. Pohl, Isotope fractionation between dissolved and suspended particulate Fe in the oxic and anoxic water column of the Baltic Sea. *Biogeosciences* **10**, 233-245 (2013).
261. M. J. Ellwood *et al.*, Iron stable isotopes track pelagic iron cycling during a subtropical phytoplankton bloom. *Proceedings of the National Academy of Sciences* **112**, E15-E20 (2015).
262. D. R. Lovley, E. J. Phillips, Novel mode of microbial energy metabolism: organic carbon oxidation coupled to dissimilatory reduction of iron or manganese. *Applied and environmental microbiology* **54**, 1472-1480 (1988).
263. D. E. Canfield *et al.*, Pathways of organic carbon oxidation in three continental margin sediments. *Marine geology* **113**, 27-40 (1993).
264. K. H. Nealson, D. Saffarini, Iron and manganese in anaerobic respiration: environmental significance, physiology, and regulation. *Annual review of microbiology* **48**, 311-344 (1994).
265. M. Vargas, K. Kashefi, E. L. Blunt-Harris, D. R. Lovley, Microbiological evidence for Fe (III) reduction on early Earth. *Nature* **395**, 65-67 (1998).
266. D. E. Canfield *et al.*, A Mesoproterozoic iron formation. *Proceedings of the National Academy of Sciences*, 201720529 (2018).
267. W. Li, B. L. Beard, C. M. Johnson, Biologically recycled continental iron is a major component in banded iron formations. *Proceedings of the National Academy of Sciences* **112**, 8193-8198 (2015).
268. E. Percak-Dennett *et al.*, Iron isotope fractionation during microbial dissimilatory iron oxide reduction in simulated Archaean seawater. *Geobiology* **9**, 205-220 (2011).
269. M. Kunzmann *et al.*, Iron isotope biogeochemistry of Neoproterozoic marine shales. *Geochimica et Cosmochimica Acta* **209**, 85-105 (2017).
270. T. M. Gibson *et al.*, Geochemical signatures of transgressive shale intervals from the 811 Ma Fifteenmile Group in Yukon, Canada: Disentangling sedimentary redox cycling from weathering alteration. *Geochimica et Cosmochimica Acta*, (2020).
271. R. C. Aller, C. Heilbrun, C. Panzeca, Z. Zhu, F. Baltzer, Coupling between sedimentary dynamics, early diagenetic processes, and biogeochemical cycling in the Amazon–Guianas mobile mud belt: coastal French Guiana. *Marine Geology* **208**, 331-360 (2004).
272. N. Planavsky *et al.*, Iron isotope composition of some Archean and Proterozoic iron formations. *Geochimica et Cosmochimica Acta* **80**, 158-169 (2012).
273. J. D. Owens *et al.*, Iron isotope and trace metal records of iron cycling in the proto-North Atlantic during the Cenomanian-Turonian oceanic anoxic event (OAE-2). *Paleoceanography* **27**, (2012).
274. A. Heimann *et al.*, Fe, C, and O isotope compositions of banded iron formation carbonates demonstrate a major role for dissimilatory iron reduction in~ 2.5 Ga marine environments. *Earth and Planetary Science Letters* **294**, 8-18 (2010).
275. O. Rouxel, E. Sholkovitz, M. Charette, K. J. Edwards, Iron isotope fractionation in subterranean estuaries. *Geochimica et Cosmochimica Acta* **72**, 3413-3430 (2008).
276. V. Busigny *et al.*, Iron isotopes in an Archean ocean analogue. *Geochimica et Cosmochimica Acta* **133**, 443-462 (2014).
277. O. J. Rouxel, A. Bekker, K. J. Edwards, Iron Isotope Constraints on the Archean and Paleoproterozoic Ocean Redox State. *Science* **307**, 1088-1091 (2005).

278. F. Kurzweil, M. Wille, N. Gantert, N. J. Beukes, R. Schoenberg, Manganese oxide shuttling in pre-GOE oceans–evidence from molybdenum and iron isotopes. *Earth and planetary science letters* **452**, 69-78 (2016).
279. K. L. Straub, B. E. Buchholz-Cleven, Enumeration and detection of anaerobic ferrous iron-oxidizing, nitrate-reducing bacteria from diverse European sediments. *Appl. Environ. Microbiol.* **64**, 4846-4856 (1998).
280. N. G. Holm, Biogenic influences on the geochemistry of certain ferruginous sediments of hydrothermal origin. *Chemical Geology* **63**, 45-57 (1987).
281. L. Hallbeck, K. Pedersen, Autotrophic and mixotrophic growth of Gallionella ferruginea. *Microbiology* **137**, 2657-2661 (1991).
282. F. Widdel *et al.*, Ferrous iron oxidation by anoxygenic phototrophic bacteria. *Nature* **362**, 834 (1993).
283. U. Schwertmann, R. W. Fitzpatrick, Iron minerals in surface environments. *Catena Supplement* **21**, 7-7 (1993).
284. S. Brake, S. Hasiotis, H. Dannelly, K. Connors, Eukaryotic stromatolite builders in acid mine drainage: Implications for Precambrian iron formations and oxygenation of the atmosphere? *Geology* **30**, 599-602 (2002).
285. D. Le Heron, M. Busfield, E. Le Ber, A. Kamona, Neoproterozoic ironstones in northern Namibia: Biogenic precipitation and Cryogenian glaciation. *Palaeogeography, Palaeoclimatology, Palaeoecology* **369**, 48-57 (2013).
286. C. Chan, D. Emerson, G. Luther III, The role of microaerophilic Fe-oxidizing micro-organisms in producing banded iron formations. *Geobiology* **14**, 509-528 (2016).
287. K. J. Thompson *et al.*, Photoferrotrophy, deposition of banded iron formations, and methane production in Archean oceans. *Science advances* **5**, eaav2869 (2019).
288. M. Llirós *et al.*, Pelagic photoferrotrophy and iron cycling in a modern ferruginous basin. *Scientific reports* **5**, 13803 (2015).
289. W. Davison, G. Seed, The kinetics of the oxidation of ferrous iron in synthetic and natural waters. *Geochimica et Cosmochimica Acta* **47**, 67-79 (1983).
290. G. K. Druschel, D. Emerson, R. Sutka, P. Suchecki, G. W. Luther III, Low-oxygen and chemical kinetic constraints on the geochemical niche of neutrophilic iron (II) oxidizing microorganisms. *Geochimica et Cosmochimica Acta* **72**, 3358-3370 (2008).
291. U. Lueder, G. Druschel, D. Emerson, A. Kappler, C. Schmidt, Quantitative analysis of O2 and Fe2+ profiles in gradient tubes for cultivation of microaerophilic Iron (II)-oxidizing bacteria. *FEMS microbiology ecology* **94**, fix177 (2018).
292. M. Schad, K. O. Konhauser, P. Sánchez-Baracaldo, A. Kappler, C. Bryce, How did the evolution of oxygenic photosynthesis influence the temporal and spatial development of the microbial iron cycle on ancient Earth? *Free Radical Biology and Medicine* **140**, 154-166 (2019).
293. S. A. Crowe *et al.*, Photoferrotrophs thrive in an Archean Ocean analogue. *Proceedings of the National Academy of Sciences* **105**, 15938-15943 (2008).
294. S. Crowe *et al.*, Deep-water anoxygenic photosythesis in a ferruginous chemocline. *Geobiology* **12**, 322-339 (2014).
295. E. Field *et al.*, Planktonic marine iron oxidizers drive iron mineralization under low-oxygen conditions. *Geobiology* **14**, 499-508 (2016).
296. E. D. Melton, E. D. Swanner, S. Behrens, C. Schmidt, A. Kappler, The interplay of microbially mediated and abiotic reactions in the biogeochemical Fe cycle. *Nature Reviews Microbiology* **12**, 797-808 (2014).
297. C. Bryce *et al.*, Microbial anaerobic Fe (II) oxidation–Ecology, mechanisms and environmental implications. *Environmental microbiology* **20**, 3462-3483 (2018).
298. S. A. Crowe *et al.*, Draft genome sequence of the pelagic photoferrotroph Chlorobium phaeoferrooxidans. *Genome Announcements* **5**, (2017).
299. Y. Qiu, T. Zhao, Y. Li, The Yunmengshan iron formation at the end of the Paleoproterozoic era. *Applied Clay Science* **199**, 105888 (2020).
300. N. Planavsky *et al.*, Iron-oxidizing microbial ecosystems thrived in late Paleoproterozoic redox-stratified oceans. *Earth and Planetary Science Letters* **286**, 230-242 (2009).
301. E. D. Swanner *et al.*, Iron isotope fractionation during Fe (II) oxidation mediated by the oxygen-producing marine cyanobacterium Synechococcus PCC 7002. *Environmental science & technology* **51**, 4897-4906 (2017).
302. L. R. Croal, C. M. Johnson, B. L. Beard, D. K. Newman, Iron isotope fractionation by Fe (II)-oxidizing photoautotrophic bacteria 1. *Geochimica et cosmochimica acta* **68**, 1227-1242 (2004).
303. W. Wu *et al.*, Fe isotope fractionation during Fe (II) oxidation by the marine photoferrotroph Rhodovulum iodosum in the presence of Si–Implications for Precambrian iron formation deposition. *Geochimica et Cosmochimica Acta* **211**, 307-321 (2017).
304. A. Kappler, C. Johnson, H. Crosby, B. Beard, D. Newman, Evidence for equilibrium iron isotope fractionation by nitrate-reducing iron (II)-oxidizing bacteria. *Geochimica et cosmochimica acta* **74**, 2826-2842 (2010).

305. N. Balci *et al.*, Iron isotope fractionation during microbially stimulated Fe (II) oxidation and Fe (III) precipitation. *Geochimica et Cosmochimica Acta* **70**, 622-639 (2006).
306. R. Guilbaud, I. B. Butler, R. M. Ellam, Abiotic pyrite formation produces a large Fe isotope fractionation. *Science* **332**, 1548-1551 (2011).
307. J. M. Rolison *et al.*, Iron isotope fractionation during pyrite formation in a sulfidic Precambrian ocean analogue. *Earth and Planetary Science Letters* **488**, 1-13 (2018).
308. S. Severmann, T. W. Lyons, A. Anbar, J. McManus, G. Gordon, Modern iron isotope perspective on the benthic iron shuttle and the redox evolution of ancient oceans. *Geology* **36**, 487-490 (2008).
309. A. W. Heard, N. Dauphas, Constraints on the coevolution of oxic and sulfidic ocean iron sinks from Archean–Paleoproterozoic iron isotope records. *Geology* **48**, 358-362 (2020).
310. K. Dideriksen *et al.*, Paleo-redox boundaries in fractured granite. *Geochimica et Cosmochimica Acta* **74**, 2866-2880 (2010).
311. M. A. Chan, C. M. Johnson, B. L. Beard, J. R. Bowman, W. Parry, Iron isotopes constrain the pathways and formation mechanisms of terrestrial oxide concretions: A tool for tracing iron cycling on Mars? *Geosphere* **2**, 324-332 (2006).
312. V. Busigny, N. Dauphas, Tracing paleofluid circulations using iron isotopes: A study of hematite and goethite concretions from the Navajo Sandstone (Utah, USA). *Earth and Planetary Science Letters* **254**, 272-287 (2007).
313. J. Sun, X. Zhu, Z. Li, Confirmation and global significance of a large-scale early Neoproterozoic banded iron formation on Hainan Island, China. *Precambrian Research* **307**, 82-92 (2018).
314. A. Mitra, H. Elderfield, M. Greaves, Rare earth elements in submarine hydrothermal fluids and plumes from the Mid-Atlantic Ridge. *Marine Chemistry* **46**, 217-235 (1994).
315. G. Steinhoefel, I. Horn, F. von Blanckenburg, Micro-scale tracing of Fe and Si isotope signatures in banded iron formation using femtosecond laser ablation. *Geochimica et Cosmochimica Acta* **73**, 5343-5360 (2009).
316. W. Li *et al.*, Contrasting behavior of oxygen and iron isotopes in banded iron formations revealed by in situ isotopic analysis. *Earth and Planetary Science Letters* **384**, 132-143 (2013).
317. N. Dauphas *et al.*, Clues from Fe isotope variations on the origin of early Archean BIFs from Greenland. *Science* **306**, 2077-2080 (2004).
318. N. Dauphas, N. L. Cates, S. J. Mojzsis, V. Busigny, Identification of chemical sedimentary protoliths using iron isotopes in the> 3750 Ma Nuvvuagittuq supracrustal belt, Canada. *Earth and Planetary Science Letters* **254**, 358-376 (2007).
319. C. D. Frost, F. von Blanckenburg, R. Schoenberg, B. Frost, S. Swapp, Preservation of Fe isotope heterogeneities during diagenesis and metamorphism of banded iron formation. *Contributions to Mineralogy and Petrology* **153**, 211 (2007).
320. E. V. Hyslop, J. W. Valley, C. M. Johnson, B. L. Beard, The effects of metamorphism on O and Fe isotope compositions in the Biwabik Iron Formation, northern Minnesota. *Contributions to Mineralogy and Petrology* **155**, 313-328 (2008).
321. J. W. Greenman, R. H. Rainbird, E. C. Turner, High-resolution correlation between contrasting early Tonian carbonate successions in NW Canada highlights pronounced global carbon isotope variations. *Precambrian Research*, 105816 (2020).
322. F. Zhang *et al.*, Oxygenation of a Cryogenian ocean (Nanhua Basin, South China) revealed by pyrite Fe isotope compositions. *Earth and Planetary Science Letters* **429**, 11-19 (2015).
323. Z. Lin *et al.*, The enrichment of heavy iron isotopes in authigenic pyrite as a possible indicator of sulfate-driven anaerobic oxidation of methane: Insights from the South China Sea. *Chemical Geology* **449**, 15-29 (2017).